MICROSTRUCTURE OF NANO AND MICRON SIZE DIAMOND-SIC COMPOSITES SINTERED UNDER HIGH PRESSURE HIGH TEMPERATURE CONDITIONS

by

Stephen Edwin Nauyoks

Bachelor of Science, 2002
New Jersey Institute of Technology
Newark, New Jersey

Master of Science, 2004
New Jersey Institute of Technology
Newark, New Jersey

Submitted to the Graduate Faculty of the
College of Science and Engineering
Texas Christian University
in partial fulfillment of the requirements
for the degree of

Doctor of Philosophy

August 2009

Acknowledgements

I would like to thank Dr. T.W. Zerda for taking me in his program and mentoring me over the years. I am truly appreciative of the experience and wonderful opportunities afforded to me by him. I am grateful for the tutelage of Dr. Ungár, Dr. Gubicza, and Dr. Palosz.

I would like to thank all of my fellow graduate students for their help and friendship.

Finally, I would like to thank my parents, my sister and brother in-law, Oma and Jim Rizzo for all of their love and support.

This work was partially funded by a NSF grant DMR 0502136. The use of the National Synchrotron Light Source at Brookhaven National Laboratory was supported by the US Department of Energy, Office of Science.

TABLE OF CONTENTS:

LIST OF TABLES

LIST OF FIGURES

CHAPTER I. INTRODUCTION

Diamonds possess many key physical properties; including exceptional hardness, wear resistance, and high thermal conductivity.[1,2] This makes them attractive for industrial applications. However, large diamonds are very expensive. Smaller diamonds, crystals with diameter sizes of micrometers and smaller, are relatively cheap, but individual diamonds this tiny would be impractical for industrial applications. Using these diamond powders to produce compacts and composites is an alternative. The large volume composites and compacts would be widely usable while still maintaining the exceptional properties of diamonds. In order to produce diamond composites, frequently SiC is used as a binding phase. These composites and compacts are produced under high pressure and high temperature conditions. These extreme conditions can vastly effect the individual crystal's microstructure. Therefore it is important to study their structure under various sintering conditions.

Crystals are collections of atoms or molecules that repeat in three dimensions. The arrangement of these atoms affects the charge distribution in the crystals. The mechanical, electrical and magnetic properties of the crystal are dependent on the charge distributions and depend on the crystallographic structure of the crystals.[3-6] Therefore, it is important to study their structure. Although it is essential to know the unperturbed structure, it is equally necessary to understand the atomic arrangement after stress and strain are introduced in the form of defects such as planar faults and dislocations. One of the most effective tools in measuring the structure of crystals is X-ray diffraction.

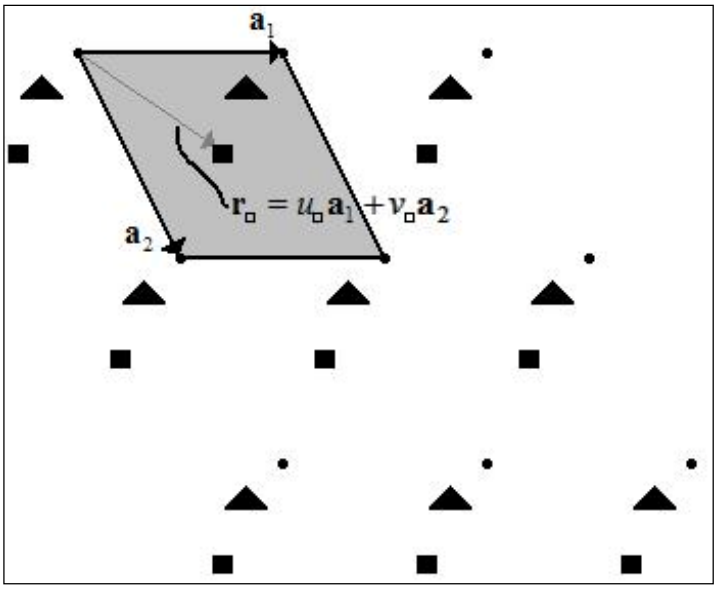

Figure 1 – An arbitrary two dimensional crystal structure. The dots represent possible lattice points, the triangles and squares are motifs, the shaded region is a possible lattice, and the vector $\mathbf{r}_{\square}$ is the position vector from the origin of the lattice to the square motif.

Before discussing structure, it is important to define the nomenclature used in crystallography. Each crystal consists of a motif. The motif can consist of a single atom or ion up to a complex molecule. Each motif must be identical in makeup, layout, and alignment. With each motif is associated a lattice point. The neighborhood of each lattice point must be in all ways identical to the neighborhood of every other lattice point. The lattice points are arranged in a three dimensional, parallel, repetitious pattern to compose the lattice. A unit cell is a parallelepiped, which when translation operations are applied can replicate the volume of the lattice.[3-6] For a two-dimensional example of a motif, lattice points, and unit cell see Figure 1. A primitive cell is a unit cell with the smallest possible volume and is defined by three crystallographic axes, $\mathbf{a}_1$, $\mathbf{a}_2$, and $\mathbf{a}_3$. The volume of the cell is

$$V = \mathbf{a}_1 \bullet \mathbf{a}_2 \times \mathbf{a}_3 . \qquad (1\text{-}1)$$

The translation from one cell to the m^{th} cell is defined as

$$\mathbf{T}_p = p_1\mathbf{a}_1 + p_2\mathbf{a}_2 + p_3\mathbf{a}_3 \tag{1-2}$$

where m_1, m_2, and m_3 are integers. If atoms in a cell are numbered 1, 2, 3…n the position to them from the origin of that cell are defined by the vectors $\mathbf{r}_1$, $\mathbf{r}_2$, $\mathbf{r}_3$… $\mathbf{r}_n$. The distance to the n^{th} atom in the m^{th} unit cell from the lattice origin is thus

$$\mathbf{R}_p^n = \mathbf{T}_p + \mathbf{r}_n \tag{1-3}$$

where $\mathbf{T}_p$ is defined in Equation (1-2).[3-7]

For reasons which will become clearer later it is important to discuss a particular type of crystallographic planes, *hkl*. These planes are equidistant from each other and parallel to each other. The first plane passes through the origin of the lattice and the next plane intercepts the three axes, $\mathbf{a}_1$, $\mathbf{a}_2$, and $\mathbf{a}_3$, at a_1/h, a_2/k, and a_3/l, respectively, see Figure 2. The three integers h, k, and l are commonly called the Miller indices.[3-7] Hereafter the symbols hkl will refer to Miller indices, when in italics they will be referring to the Miller planes, and when bracketed by < > they will indicate a direction.

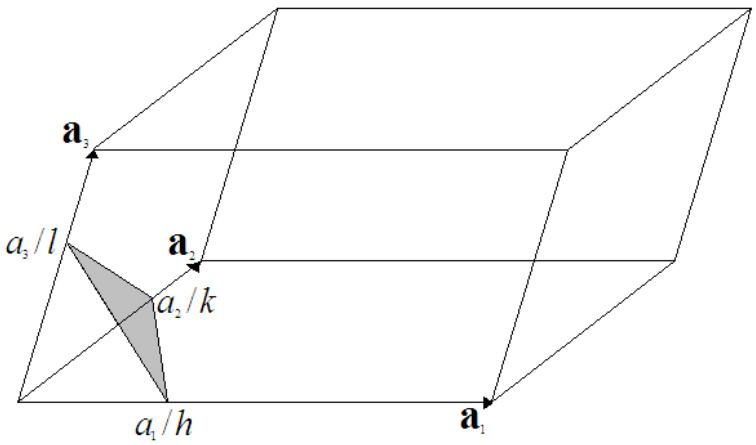

Figure 2 – An arbitrary lattice with a highlighted plane with Miller indices h, k, and l.

A vector $\mathbf{H}_{hkl}$ which is perpendicular to the planes and with a magnitude which is the reciprocal of the distance between the planes will now be introduced. Just as we defined the crystallographic axes $\mathbf{a}_1$, $\mathbf{a}_2$, and $\mathbf{a}_3$, we can define three reciprocal vectors $\mathbf{b}_1$, $\mathbf{b}_2$, and $\mathbf{b}_3$ by:

$$\mathbf{b}_1 = \mathbf{a}_2 \times \mathbf{a}_3 / \mathrm{V}, \quad \mathbf{b}_2 = \mathbf{a}_3 \times \mathbf{a}_1 / \mathrm{V}, \quad \mathbf{b}_3 = \mathbf{a}_2 \times \mathbf{a}_2 / \mathrm{V} \tag{1-4}$$

where V was defined by Equation (1-1). There is an orthonormal relationship between the crystallographic axes and the reciprocal axes, that is[7]:

$$\mathbf{a}_i \bullet \mathbf{b}_j = \begin{cases} 1 & i = j \\ 0 & i \neq j \end{cases} . \tag{1-5}$$

The vector $\mathbf{H}_{hkl}$ can be defined using the Miller indices and the reciprocal axes:

$$\mathbf{H}_{\mathrm{hkl}} = \mathrm{h}\mathbf{b}_1 + \mathrm{k}\mathbf{b}_2 + \mathrm{l}\mathbf{b}_3 . \tag{1-6}$$

To show that $\mathbf{H}_{hkl}$ is perpendicular to the crystallographic planes it is sufficient to verify that it is perpendicular to two vectors which are parallel to that plane. One can use the two vectors: $\frac{\mathbf{a}_1}{\mathrm{h}} - \frac{\mathbf{a}_2}{\mathrm{k}}$ and $\frac{\mathbf{a}_2}{\mathrm{k}} - \frac{\mathbf{a}_3}{\mathrm{l}}$. In order to demonstrate the normality of those vectors one must confirm that the dot product is zero by using the orthonormal relationship in Equation (1-5).[7]

To show that the magnitude of $\mathbf{H}_{hkl}$ is the reciprocal to the spacing we must notice that the spacing between adjacent planes is:

$$\mathrm{d}_{hkl} = \frac{|\mathbf{a}_1|}{\mathrm{h}} \cos\phi = \frac{\mathbf{a}_1}{\mathrm{h}} \cdot \mathbf{n} , \tag{1-7}$$

where d_{hkl} is the spacing between planes, **n** is a unit vector normal to the planes, and φ is the angle between the $\mathbf{a}_1$ axis and the vector **n**. Since $\mathbf{H}_{hkl}$ is normal to the planes we can use it to define **n**, that is $\mathbf{n} = \mathbf{H}_{hkl} / |\mathbf{H}_{hkl}|$. Using the definition of $\mathbf{H}_{hkl}$ in Equation (1-6) and the orthonormal relation in Equation (1-5) it is easy to see that[7]:

$$d_{hkl} = \frac{1}{|\mathbf{H}_{hkl}|}. \tag{1-8}$$

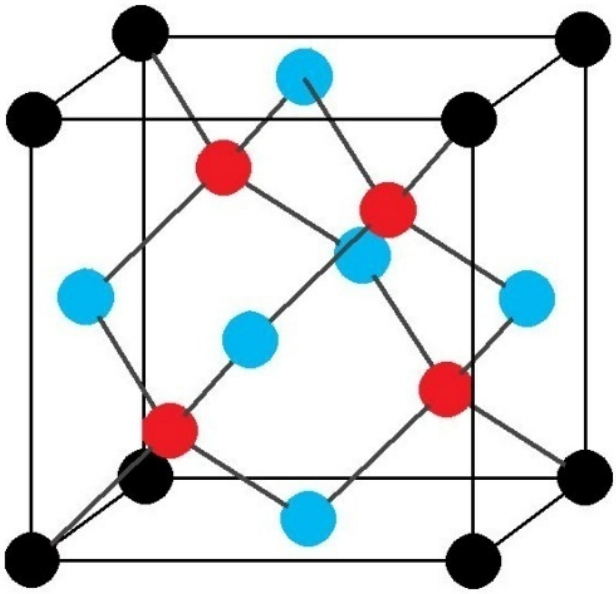

Figure 3 – The diamond crystal structure. Note, the black spheres represent carbon atoms on the corners, the red spheres represent interior carbon atoms, and the blue spheres represent carbon atoms on the surface. The grey lines connect the four nearest neighbors.

The lattice of a diamond is face-centered cubic. A face-centered cubic has an eighth of a lattice point at each corner of a cube and half of a lattice point centered at each face. The diamond structure has two identical face-centered cubics with lattices anchored at (0,0,0) and (¼,¼,¼). The primitive cell is chosen such that it has eight carbon atoms. The locations of the carbon atoms are: (0,0,0), (1/2,1/2,0), (1/2,0,1/2), (0,1/2,1/2),

(1/4,1/4,3/4), (1/4,3/4,1/4), (3/4,1/4,1/4), and (3/4,3/3,3/4). That is one at the corner, one in the middle of three of the sides, and four inside the cube, see Figure 3. Each carbon atom has a tetrahedral binding to its four nearest atoms. It has twelve next nearest atoms. The carbon atoms are covalently bound to each other. The diamond structure is mostly empty with a maximum packing space of hard spheres being 34%.[6]

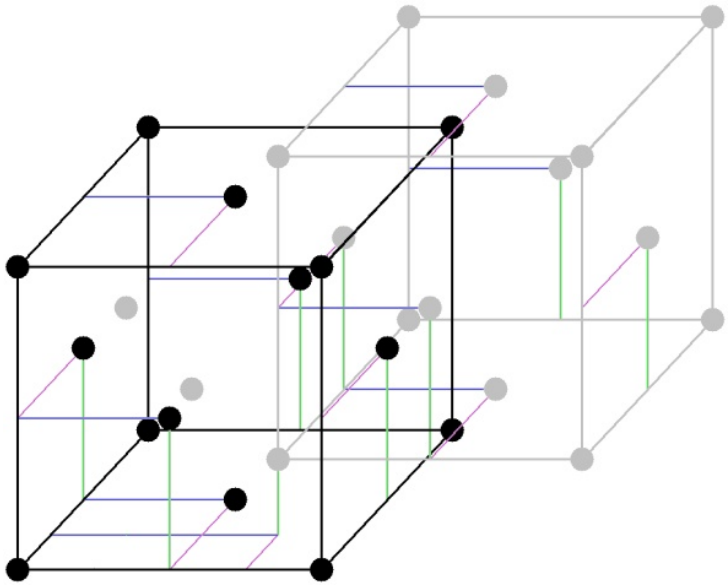

Figure 4 – The diamond structure can be considered as two face-centered cubic structures, one offset from the other by ¼ of the length of each lattice vector. The color lines exist to help lead the eye.

The diamond structure is composed of two face-centered cubic structures displaced by a quarter of the length of each axis, see Figure 4. If instead of having identical atoms in both of these face-centered cubic structures there were two different motifs associated with each face centered cubic lattice then it would be the zincblende structure, see Figure 5. This is the structure that the SiC forms in the production of diamond-SiC composites. The cubic form of SiC is face-centered cubic, with the motif of each lattice point consisting of a carbon atom and a silicon atom. There are four molecules of SiC per unit cell. The lattice

points are found at (0,0,0), (1/2,1/2,0), (1/2,0,1/2) and (0,1/2,1/2). There is a lattice point in the corner and one in the middle of 3 of the faces. Each atom has four nearest neighbors of the opposite variety.[4,6] SiC can also form in a hexagonal structure, but that was not found in any of the samples I prepared, which was confirmed by X-ray diffraction analysis.

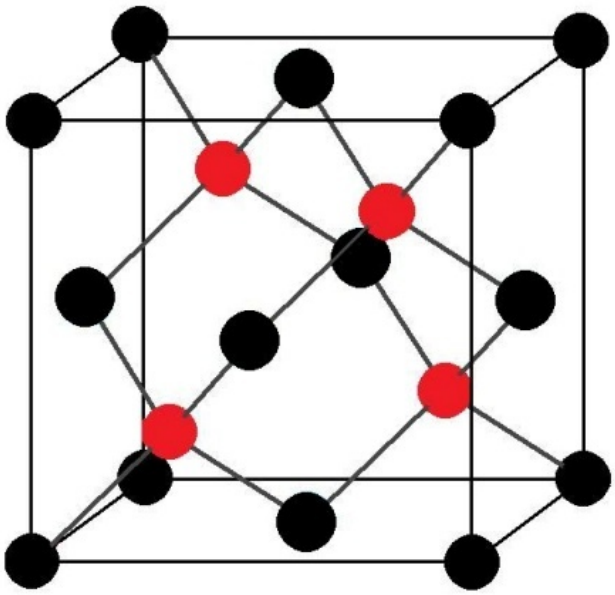

Figure 5 – The SiC structure. Each red sphere represents a silicon atom and each black sphere represents a carbon atom.

Plastic deformation occurs in crystals in the form of slips. A slip is when part of a crystal moves along a bordering part of the crystal. The surface of the slip is called the slip plane and the direction of motion is known as slip direction. Because slips cause the rearrangement of atoms, slips are anisotropic and depend on the lattice structure.

If the displacement of the atoms after a slip is equal to a translation vector the overall structure of the crystal will remain unchanged. However, in face-centered cubic crystals if the displacement is not equal to the translation vector a stacking fault is formed. The lattice points can be represented by closed packed spheres. A plane of these closed

packed spheres can be assembled centered over an arbitrary point called A, see Figure 6. The next layer of closed packed spheres can be assembled centered over the same point A, or over one of two saddle points between the spheres, called B and C. A crystal is created with a repeated stacking sequence. For a face-centered cubic lattice the stacking sequence is ABCABC…. However, due to partial displacements sometimes there are errors in these sequences. To help better visualize stacking faults the Shockley notation will be introduced. A step from $A \to B$, $B \to C$, or $C \to A$ is represented with a Δ, whereas a step from $A \to C$, $C \to B$, or $B \to A$ is represented with a ∇. The face-centered cubic structure can then be represented by $\Delta\Delta\Delta \ldots$.[4]

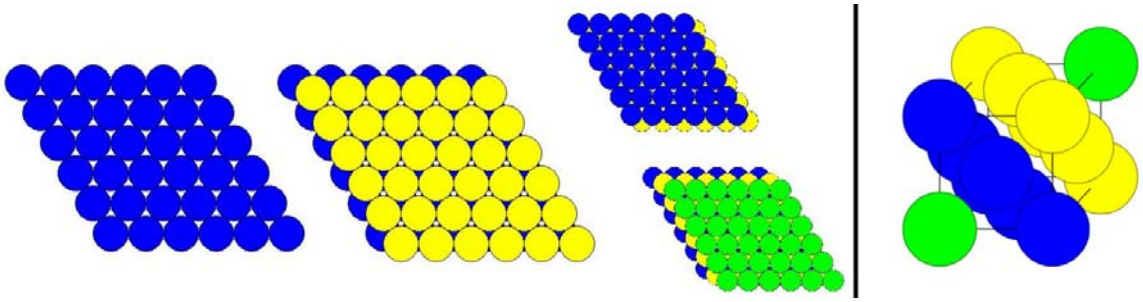

Figure 6 – Left: The closed packed packing sequence viewed from the top. The first row of closed packed spheres is placed over A, the next row is placed over B, and the third row can be placed over A, top, which is the hexagonal closed packed structure or over C, bottom which is the face-centered cubic structure. Right: A side view of the ABC stacking sequence in the <111> direction.

A stacking fault can be formed one of three ways: a) One set of planes can slip between its original saddle point to a different saddle point, for example a plane centered over B can slip to C. Then each plane to one side of the slip would be in a new location, A to B, B to C, and C to A. The stacking sequence would then be ABCACAB or $\Delta\Delta\Delta\nabla\Delta\Delta$. b) A plane can be removed and the subsequent gap closed. For example if a B plane was removed the stacking sequence would be ABCACAB which is the same as example (a).

These two examples are called intrinsic stacking faults. c) An additional plane can be placed between two success planes. For example an A plane can be placed between a B and C plane to get ABCABACA or $\Delta\Delta\Delta\Delta\nabla\nabla\Delta$. This example is known as an extrinsic stacking fault.[4]

Twinning is when a partial displacement occurs on successive neighboring planes, see Figure 7. For example a face-centered cubic crystal with 8 planes would have a stacking sequence of $A_1B_2C_3A_4B_5C_6A_7B_8$. (Note the subscripts are only to distinguish between layers of the crystal.) If a partial displacement which causes the fifth layer to slip from B to C were to occur the new stacking sequence would be $A_1B_2C_3A_4C_5A_6B_7C_8$ or $\Delta\Delta\Delta\Delta\nabla\Delta\Delta\Delta$. Next, if a similar partial displacement were to occur at the sixth plane the stacking sequence would be $A_1B_2C_3A_4C_5B_6C_7A_8$ or $\Delta\Delta\Delta\Delta\nabla\nabla\Delta\Delta$. If this pattern of partial slips would continue to happen along each successive plane the final stacking sequence would be $A_1B_2C_3A_4C_5B_6A_7C_8$ or $\Delta\Delta\Delta\Delta\nabla\nabla\nabla\nabla$. This is twinning. Note that the ABAB sequence is the hexagonal close-packed stacking sequence. Both stacking faults and twinning introduce a fault that mimics the hexagonal stacking sequence.[4]

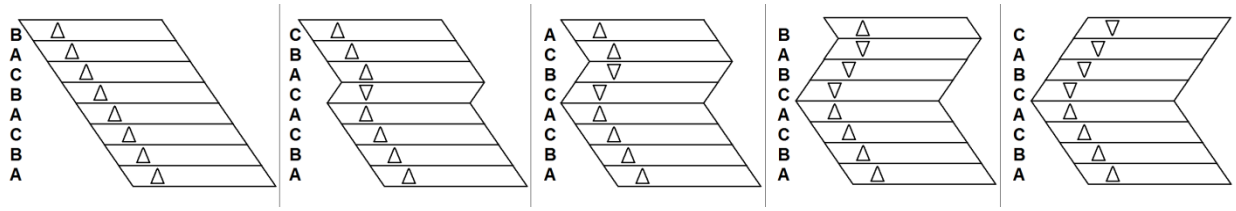

Figure 7 – The sequence from left to right of stacking faults which will lead to a twinned face-centered cubic crystal.

One can envision a coherent glide between two adjacent atomic planes. If the distance between the planes is a and the instantaneous difference between planes is x, the stress, σ, will be a periodic function of x with period of b, the distance between atoms in the direction of the glide. A simple equation for the stress in terms of the shear modulus which satisfies the periodicity requirements and Hooke's law is:

$$\sigma = \frac{\mu b}{2\pi a} \sin 2\pi \frac{x}{b} . \tag{1-9}$$

The stress necessary for a glide would be on the order of $\mu/2\pi$. By this approximation a nickel wire with a cross sectional area of 1 mm^2, with a shear modulus of about 8×10^{10} $N\bullet m^{-2}$, would be able to suspend a 1400 kg mass without permanent damage. From practice we know this is not even close to true. The enormous difference in measured shear stress and calculated stress found from Equation (1-9), lies in the assumption that adjacent planes coherently glide. Instead, atomic movement through the lattice takes place by way of the propagation or glides of dislocations.[6,8]

Dislocations unlike stacking faults, which are planar or two dimensional defects, are linear defects. There are two types of dislocations to consider, screw and edge. The screw dislocation is when the dislocation is parallel to the slip vector, see Figure 8. One can picture the ramp in a parking garage to visualize a screw dislocation. One can also imagine partially cutting a crystal in half with a knife, the cut being perpendicular to the edge of the crystal. A shear stress applied parallel to the cut would produce a screw dislocation. An edge dislocation is perpendicular to the slip vector, see Figure 9. It can also be considered as adding a half plane of atoms above the slip plane. The dislocation

would then be along the edge of where the plane ends. A dislocation can also be a combination of edge and screw.[6,8]

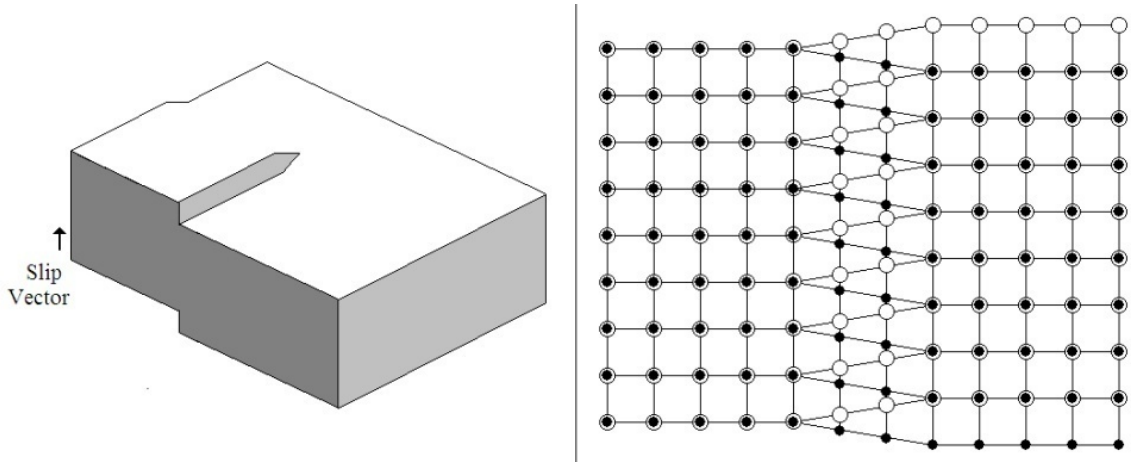

Figure 8 – The figure on the left shows a slip that produces a screw dislocation. The figure on the right is a possible arrangement of atoms that can produce a screw dislocation. The open circles represent atoms out of the page while the closed circles represent atoms in the page.

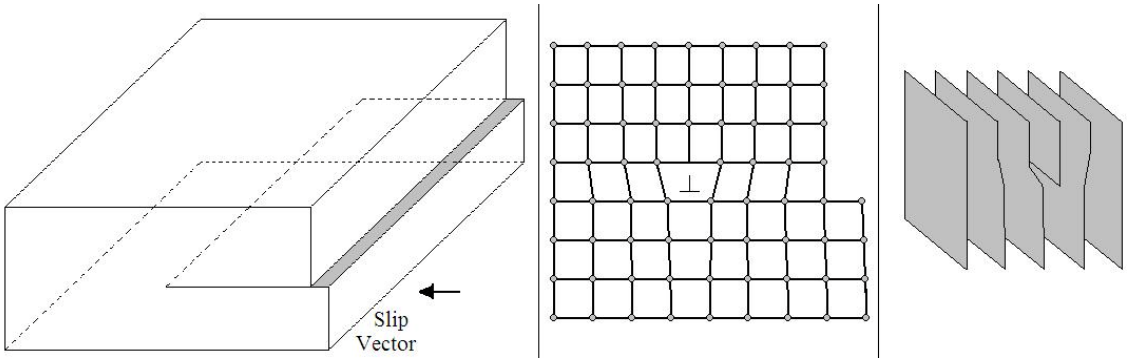

Figure 9 – The figure on the left shows a slip that produces an edge dislocation. The middle figure shows an approximate arrangement of the atoms. The figure on the left illustrates how an edge dislocation can be created by adding a partial plane in-between two other planes.

Outside the core of the dislocation the force to compress the atoms or stress falls off at 1/r, where r is the distance to the dislocation. Therefore it is hard to additionally

compress atoms very near to a dislocation and the effects of the dislocation are minimal further away. Integrating the stress gives the energy of the dislocation as a function of ln(r). Because the stress around the dislocation decreases with distance as 1/r there needs to be an inner limit or an inner cut-off radius for the stress, otherwise the equation would approach infinity as r approaches 0. Likewise if there were no outer limit or outer cut-off radius, to find the total energy of a dislocation one would integrate ln(r) over infinity which would give infinite energy.[6,8]

In order to see how slips can propagate through the movement of dislocations, see Figure 10. In Figure 10 (a) an edge dislocation was created by adding a half plane of atoms for the arrangement found in the top. The line dislocation is located directly beneath the half plane of atoms and is coming out of the page. If a stress is applied it can cause an atomic rearrangement like that found in (b). Now the dislocation is in-between the two adjacent half planes. The arrangement in (b) is not stable so the atoms may rearrange themselves into the stable pattern found in (c). Investigation of the image shows that from the top image to the bottom image the half plane of atoms and thus the dislocation have all moved one interatomic distance to the right. Instead of requiring coherent glide among planes deformation can be brought about by the movement of line defects.

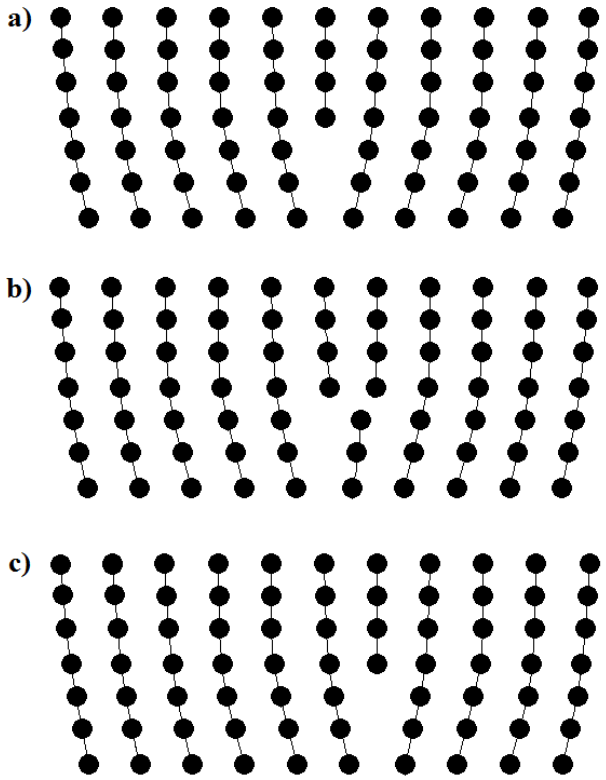

Figure 10 – From top to bottom: glide in a crystal brought about from the movement of an edge dislocation.

A convenient way of classifying dislocations is with the Burgers vector. A Burgers vector is created by drawing what should be a closed loop around the dislocation. Because the loop surrounds a dislocation it will not finish where it started. The vector that connects the beginning of the loop and the end is the Burgers' vector. In an edge dislocation the Burgers vector is perpendicular to the dislocation line. In a screw dislocation the Burgers vector is parallel to the dislocation.[6,8]

CHAPTER II. THEORETICAL FRAMEWORK

X-ray diffraction is a significant tool in analyzing the microstructure of the crystals. X-ray diffraction uses the wave nature of light. Differences in path length will lead to differences in phases. Differences in phases lead to the change in the amplitude of the reflected beam. The amplitude of the reflected beam is dependent on whether the differences in path length are integer multiples of the wavelength, which will lead to total constructive interference, or whether they are not which will lead to destructive interference. The amplitude of the reflected beam will be at a maximum if there is total constructive interference and at a minimum when there is total destructive interference.

The periodic arrangement of atoms in a crystal implies that each set of the previously discussed *hkl* planes in the crystals will be equally spaced. W. L. Bragg assumed that these planes acted like silver mirrors and the X-rays reflected specularly, that is the incident angle is equal to the diffracted angle. This led to the equation which is named after him:

$$n\lambda = 2d_{hkl} \sin\theta \qquad (2\text{-}1)$$

where, n is an integral multiple, λ is the wavelength, d_{hkl} is the spacing between the *hkl* planes, and θ is the incident angle. In Figure 11 one can see that $2d_{hkl} \sin\theta$ is the difference in path length between two adjacent planes. We know that there is total constructive interference only if the path difference is equal to an integral multiple of the wavelength. Bragg's equation assumes that there is elastic collision between the atoms and the X-ray radiation and that each plane only partially reflects the incident radiation.[4,5,7]

Since there is equivalence between the first order *2h2k2l* plane and the second order *hkl* planes, etc, the n is often dropped in Bragg's equation. Also note that $\sin\theta \leq 1$. This implies that $\lambda \leq 2d_{hkl}$. Since d_{hkl} is on the order of angstroms for a typical crystal, the wavelength must also be on the order of angstroms. Bragg's equation would not work for visible light on most crystals.

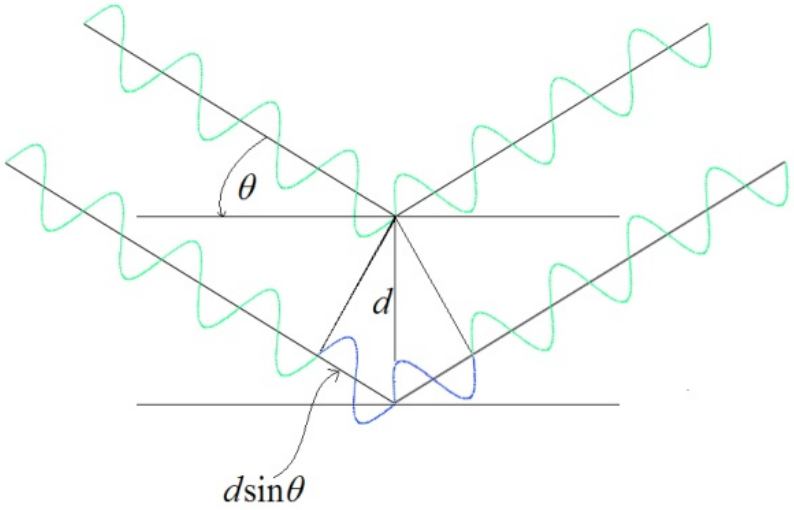

Figure 11 – The path difference between the top wave and bottom wave is 2dsinθ.

The distance between the origin and a plane is $\mathbf{n}\bullet\mathbf{r} = d$, where **n** is a unit vector normal to the plane, which was already defined as $\mathbf{n} = \mathbf{H}_{hkl} / |\mathbf{H}_{hkl}|$ and **r** is a vector from the origin to the plane. The **r** vector for a cube with side length of a is $\mathbf{r} = a(1/h\mathbf{a}_1 + 1/k\mathbf{a}_2 + 1/l\mathbf{a}_2)$. Using the orthonormal relationship defined in Equation (1-5), one can see that:[7]

$$d_{hkl} = \frac{a}{\left(h^2 + k^2 + l^2\right)^{1/2}} \qquad (2\text{-}2).$$

Bragg's equation can also be written in vector form, that is $\frac{\mathbf{s}-\mathbf{s}_0}{\lambda}=\mathbf{H}_{hkl}$, where **s** and $\mathbf{s}_0$ are the unit vectors in the direction of the incident beam and reflected beam. Ewald's sphere or the sphere of reflection is a way to represent Bragg's equation graphically. The vector $\mathbf{s}_0/\lambda$ is drawn parallel to the incident beam and terminates at the origin of reciprocal lattice. A sphere of radius $1/\lambda$ is drawn around the point where the vector $\mathbf{s}_0/\lambda$ originated. Any point where the sphere intersects a point *hkl* represents a set of *hkl* planes which satisfy Bragg's equation. The vector from the origin to *hkl* is $\mathbf{H}_{hkl}$. The diffracted beam will be in the direction of the vector $\mathbf{s}/\lambda$ which originates where $\mathbf{s}_0/\lambda$ originates and terminates where $\mathbf{H}_{hkl}$ terminates, thus satisfying Bragg's equation, see Figure 12.[7]

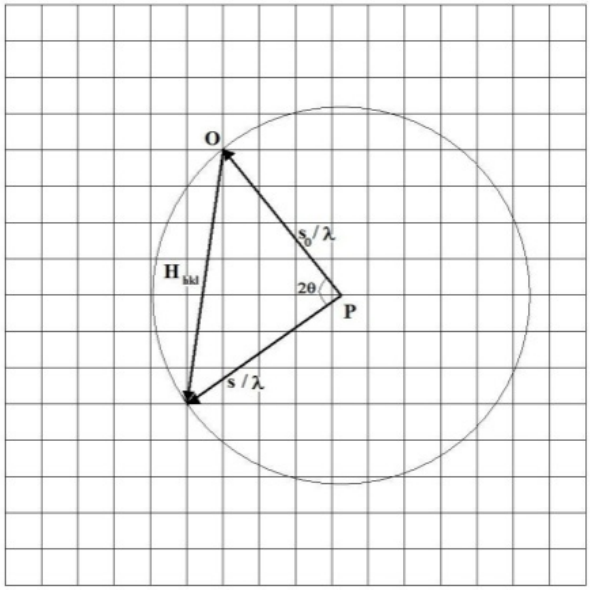

Figure 12 – An example of a two dimensional Ewald sphere. The incident beam is directed along the vector s_0/λ, H_{hkl} is the reciprocal vector which terminates on *hkl*, s/λ is the vector directed along the reflected beam, O is the origin of the reciprocal lattice, and P is the center of the sphere.

Because this study involves small crystals it would be impractical to measure individual crystals. Instead, powder diffraction techniques were used. The sphere of reflection would demonstrate points where a single crystal would reflect a beam. However, multiple crystals, with random orientations, were measured. The crystals would then be randomly rotated about the origin. This would cause the points of reflection to be rotated about an axis. This would in turn create a diffraction pattern with a circular shape. This explains why crystal alignment did not need to be performed before measurement.

The scattering of X-rays is done by the electrons surrounding the atoms. It is therefore important to compare the arrangement of the atoms in the lattice to see what path differences arise, see Figure 13. These path differences will determine the intensity of the beam. This phase difference is expressed by the structure factor F_{hkl}, which is the ratio of the amplitudes scattered by the atoms in the cell to that of a single electron. This number can be expressed in complex form as:

$$F_{hkl} = \sum_{n=0}^{n=N} f_n e^{2\pi i \mathbf{r}_n \cdot \mathbf{H}} \tag{2-3}$$

where, f_n is the atomic scattering factor, $2\pi i \mathbf{r}_n \cdot \mathbf{H}$ is the phase angle, and $\mathbf{r}_n$ is the position of the n^{th} atom. If the arrangement of the atoms in the lattice causes the structure factor to be zero for a certain set of hkl indices there will be no diffracted beam even if Bragg's equation is satisfied.[6]

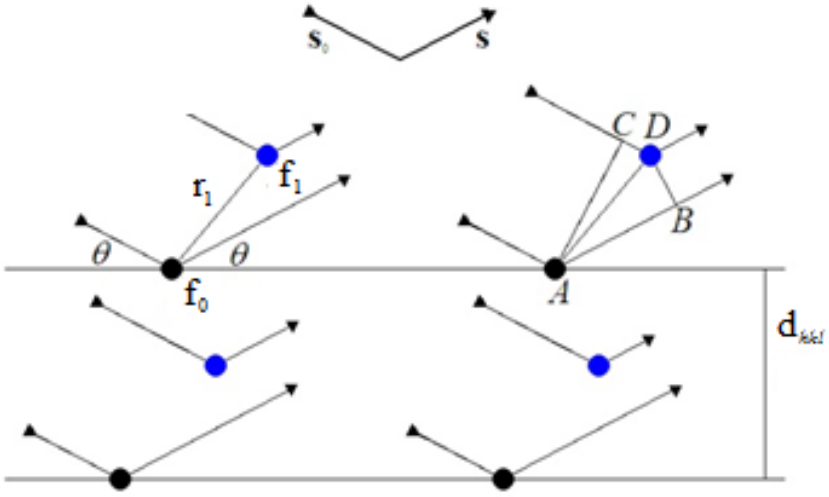

Figure 13 – A crystal with atomic scattering of f_o in some *hkl* plane. There is another atom with atomic scattering of f_1 a distance r_1 away. The path difference between the two reflected beams is AB-CD.

Using Equation (2-3) and the position of the atoms in the diamond structure one can see that the structure factor is,

$$F_{hkl} = 1 + e^{i\pi(h+k)} + e^{i\pi(h+l)} + e^{i\pi(k+l)} + e^{i\pi/2(h+k+3l)} + e^{i\pi/2(h+3k+l)} + e^{i\pi/2(3h+k+l)} + e^{3i\pi/2(h+k+l)}. \quad (2\text{-}4)$$

Unless h, k, and l are all odd or all even and h + k + l = 4n, Equation (2-4) will be zero and no reflected beam will be observed. Similarly, the selection rules for SiC require that h, k, and l be either all odd or all even.[6] Even though the diamond structure and the SiC structure are both face-centered cubic with lattice constants of the same magnitude, because the arrangement of the atoms in the crystal diamond has stricter selection rules less diffraction peaks can be found in the diamond's diffraction patterns than in SiC's pattern. The more restrictive selection rules for diamond limit the number of reflections for a given wavelength. In order to increase the number of peaks it is necessary to use an X-ray source with a smaller wavelength.

It might be expected that X-ray diffraction patterns consist of strong delta like functions that exist only at angles that satisfy Bragg's equation. In practice it is quickly seen that this is not the case. The peaks have broadening which can be due to the finite size of the crystallites, crystal defects, including stacking faults and dislocations, internal stress in the crystals, a non-monochromatic beam, and instrumental broadening.[4,5,7]

Most X-ray tubes use a metal anode, frequently it is copper. Copper emits two strong characteristic X-ray wavelengths, K_{α_1} and K_{α_2}. The two wavelengths have similar values and therefore have similar Bragg angles.[4,5,7] If broadening from other sources is limited, for example if the crystals are relatively large, there will be enough separation between the peaks and the interference they cause each other can be eliminated numerically. Also, the effects of K_{α_2} can be limited by thoroughly filtering the source. This however could greatly reduce the intensity of K_{α_1}. One way to increase the intensity would be to increase the power supplied to the anode. Increased power, could overheat the anode. To avoid overheating, a rotating anode which can be cooled more effectively is often used. Another solution is to use a synchrotron light source, which is a very intense light source which can be strongly filtered leading to an almost monochromatic beam.

As was mentioned before, the powder diffraction patterns are circular. The radius is small for small angles of incidence. A rectangular detector measuring circular diffraction patterns does lead to instrumental broadening which is typically asymmetrical with respect to the diffraction angle. The measured intensity is a convolution of the instrumental function with the real band shape function. When the instrumental

broadening is known, the real band shape can be found by the deconvolution Fourier transform method.

Near the Bragg angle, the plane that destructively interferes with the first plane is deep within the crystal. The plane that destructively interferes with the second plane is even deeper within the crystal. If the crystallite is small, not all of the planes inside the crystal will have another plane that destructively interferes with them. This leads to only partial destructive interference and the broadening of the diffracted peak. The smaller the crystallite is the more planes that lack an out of phase counterpart there will be. Therefore the broadening will be more pronounced.[5]

One way of estimating the crystallite size is by using the Scherrer method. In a crystal with length t and m planes there will be an angle θ_B which satisfies the Bragg equation, see Figure 14. There are two limiting angles θ_1 and θ_2 such that any incident angle greater than θ_2 and less than θ_1 will not have total destructive interference. The surface plane destructively interferes with the middle plane. So, a ray incident on the surface at an angle of θ_1 will be $(m+1)$ wavelengths out of phase with ray incident on the last plane, m. Likewise a ray incident on the surface at an angle of θ_2 will be $(m-1)$ wavelengths out of phase with a ray incident on the last plane. Bragg's equation is satisfied for these two angles if:

$$2t\sin\theta_1 = (m+1)\lambda \qquad (2\text{-}5)$$

$$2t\sin\theta_2 = (m-1)\lambda \qquad (2\text{-}6)$$

The Scherrer formula can be derived using Equations (2-5) and (2-6) and some algebraic manipulation:

$$t = \frac{0.9\lambda}{B\cos\theta_B} \tag{2-7}$$

where $B = \frac{1}{2}(\theta_1 - \theta_2)$. B is the full width at half maximum (FWHM) of the peak which has a maximum at θ_B. For reference suppose that $\theta_B = 40^o$, $\lambda = 0.154$ nm, and d = 0.1 nm. A crystal 0.5 mm in diameter would have 5×10^6 parallel lattice planes and an estimated, using Equation (2-7), FWHM value of 2×10^{-5} °, which is immeasurable. By contrast, a crystal that is 30 nm in diameter would only have 300 parallel lattice planes and an estimated FWHM value of 0.3^o, which is easily detectable.[5]

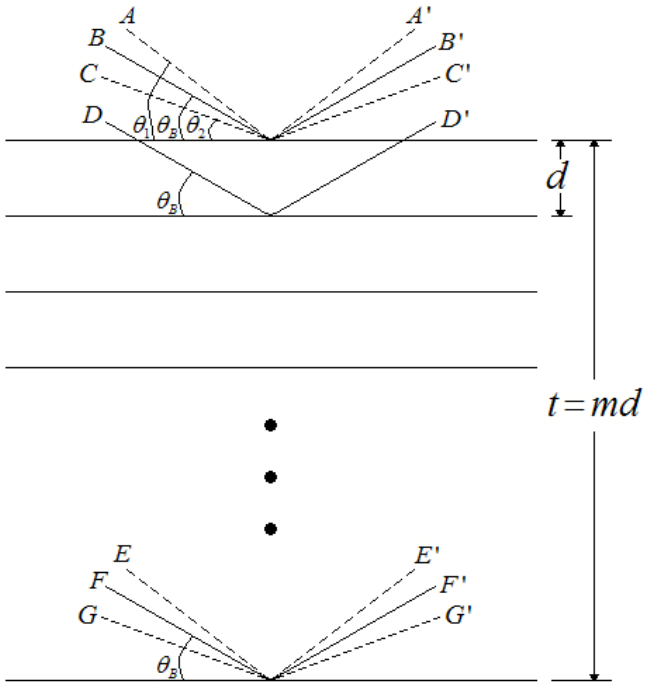

Figure 14 – The primed letters represent diffracted beams. In this incidence θ_B is the angle at which Bragg's equation is satisfied. The diffracted beam B', D' and F' will all be in phase with each other and constructively interfere.

The Scherrer method only takes into consideration broadening due to crystallite size. Also, since defects like stacking faults and dislocations affect the space between atoms they can cause profile broadening as well. A more sophisticated technique must be used to account for each of these effects. For this research the extended Convolution Multiple Whole Profile (eCMWP) method was used.

The eCWMP method assumes that the experimental profile is the sum of the background and the convolution of the size profile, I^S, the dislocation profile, I^D, the stacking fault profile, I^{SF}, and the instrumental profile, I^{inst}:

$$I^{exp} = I^S * I^D * I^{SF} * I^{inst} + \text{background} \tag{2-8}$$

the star denotes convolution. The profile stripped of instrumental broadening and background, I^F, would then be the convolution of I^S, I^D, and I^{SF}: $I^F = I^S * I^D * I^{SF}$. The Fourier transform of this equation is:

$$A_L = A_L{}^S A_L{}^D A_L^{SF} \tag{2-9}$$

the superscripts S, D and SF indicate size, dislocation, and stacking faults, respectively and L represents the Fourier variable.[9-11] The difficulties in solving Equation (2-9) is in how the Fourier size coefficient, $A_L{}^S$, the distortion effect due to dislocations, $A_L{}^D$, and the Fourier planar fault coefficient, A_L^{SF}, are treated.

Recall, that the Sherrer method, Equation (2-7), showed that the peak profile is dependent on the size of crystallite. Guinier and Bertaut showed that the intensity distribution for a given set of *hkl* planes due to the size distribution of a crystal powder is a Fourier transform of a volume function, V(t), where V(t) is the volume shared by the

crystal and its "double" divided by the volume of the crystal, V.[12,13] The "double" is found by taking a translation of length t normal to the *hkl* planes. Since V(t) is a Fourier transform of the intensity profile, if one were to find the function V(t) they could find A_L^S, which is the Fourier size coefficient in Equation (2-9).

The volume function, V(t) can be found by dividing the crystal into cylinders, see Figure 15, and integrating over those cylinders. The crystal has a thickness of M, t is the length of the translation which is normal to the lattice planes *hkl*, and the cylinder has a cross sectional area of $d\sigma_M$. One can clearly see in Figure 15 that the length of the cylinder is M – t as long as the translation is less than thickness and there is no shared volume if the translation is greater than the thickness. The volume function V(t) would therefore be:

$$V(t) = \frac{1}{V}\int_{M=0}^{M=\infty} \left(M - |t|\right) d\sigma_M \,. \tag{2-10}$$

If the translation is greater than the thickness of the crystal there will be no shared volume between the crystal and its "double", therefore the lower limit of integration in Equation (2-10) can be changed to M = t. Some algebraic manipulations can also be done to achieve the following equation:

$$V(t) = \int_{|t|}^{\infty}\left(1 - \frac{|t|}{M}\right)\frac{M}{V} d\sigma_M = \int_{|t|}^{\infty}\left(1 - \frac{|t|}{M}\right) g(M)\, dM \tag{2-11}$$

where g(M) is the distribution of the column heights.[13] The beauty in using g(M) in Equation (2-11) is that it can be easily used even if the crystallites are not identical. The eCMWP method assumes that the volume size distribution is log-normal and that the shapes of the crystallites are spheres. This reduces Equation (2-11) to:

$$A^S(t) = \int_{|t|}^{\infty} \left(1 - \frac{|t|}{M}\right) M^2 \left[\int_M^{\infty} f(x)dx\right] dM \tag{2-12}$$

where $f(x)$ is the log-normal size distribution density function which is:

$$f(x) = \frac{1}{(2\pi)^{1/2}\sigma x} \exp\left[\frac{-(\log(x/w))^2}{2\sigma^2}\right] \tag{2-13}$$

where σ is the variance and w is the median.[10,14] The area-weighted mean crystallite size is therefore:[14]

$$\langle x \rangle_{area} = we^{2.5\sigma^2}. \tag{2-14}$$

One can find similar expressions for the volume-weighted mean and arithmetically weighted mean but these were not used and all the size values listed are the area-weighted mean.

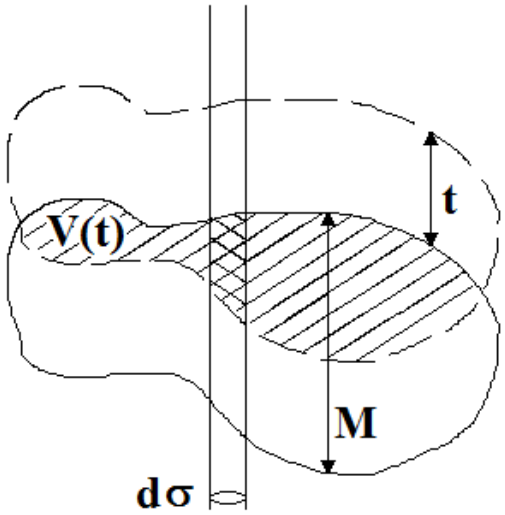

Figure 15 – A cross sectional view of a crystal and its double. The solid figure is the crystal with thickness of M. The dashed figure is the crystal's "double" translated by a distance of t. The hatched region is the volume V(t). The double hatched region is the volume shared by V(t) and the cylinder, which has a cross sectional area of dσ.

The Fourier coefficient due to dislocations was found by using the Warren-Averbach method. The coefficient can be expressed as:

$$A_L{}^D = \exp\left(-2\pi^2 g^2 L^2 \left\langle \varepsilon_L^2 \right\rangle\right) \tag{2-15}$$

where L is the Fourier transform variable, g is the magnitude of the diffraction vector, and $\left\langle \varepsilon_L^2 \right\rangle$ is the mean square strain, which depends on how much the atoms are displaced due to strain compared to an ideal lattice arrangement.[15] Krivoglaz developed a method to calculate the mean square strain caused by dislocations.[16] Wilkens improved Krivoglaz's method by assuming that dislocations have an outer cutoff radius, R_e^*.[17] Recall that the total energy of a dislocation would go to infinity if an outer cut-off radius is not considered. Krivoglaz just let the outer cut-off radius be the radius of the crystal. Wilkens introduced the outer cut-off radius parameter as R_e^*. Using this parameter Wilkens derived the following equation for the mean strain:

$$\left\langle \varepsilon_L^2 \right\rangle = \left(\frac{b}{2\pi}\right)^2 \pi\rho C f\left(L / R_e^*\right) \tag{2-16}$$

where b is the magnitude of the Burgers vector, C is the contrast factor of the dislocations and $f(\ )$ is Wilkens function of strain as defined by:

$$f^*(\eta) = -\log\eta + \left(\frac{7}{4} - \log 2\right) + \frac{512}{90}\frac{1}{\pi}\frac{1}{\eta} + \frac{2}{\pi}\left(1 - \frac{1}{4\eta^2}\right)\int_0^\eta \frac{\arcsin V}{V} dV$$

$$-\frac{1}{\pi}\left(\frac{769}{180}\frac{1}{\eta} + \frac{41}{90}\eta + \frac{2}{90}\eta^3\right)\left(1-\eta^2\right)^{1/2}$$

$$-\frac{1}{\pi}\left(\frac{11}{12}\frac{1}{\eta^2} + \frac{7}{2} + \frac{1}{3}\eta^2\right)\arcsin\eta + \frac{1}{6}\eta^2, \ \eta < 1$$

$$f^*(\eta) = \frac{512}{90}\frac{1}{\pi}\frac{1}{\eta} - \left(\frac{11}{24} + \frac{1}{4}\log 2\eta\right)\frac{1}{\eta^2}\ ,\ \eta \geq 1 \tag{2-17}$$

where $f\left(L/R_e^*\right) = f^*(\eta)$ where $\eta = (1/2)\exp(-1/4)\left(L/R_e^*\right)$.[10,17] The anisotropy of the dislocations is accounted for by the average contrast factor C.[18] In a cubic crystal C is dependent on C_{h00}, the average contrast factor in the <h00> direction, which is dependent on the elasticity of the material and on the fourth-order polynomial of the hkl indices. The average contrast factor therefore is[10]:

$$C = C_{h00}\left(1 - q\frac{h^2k^2 + h^2l^2 + k^2l^2}{\left(h^2 + k^2 + l^2\right)^2}\right). \tag{2-18}$$

In order to determine the Fourier coefficient due to planar faults the magnitude of peak broadening and peak location were first evaluated. Diffraction peaks were numerically calculated using the program: DIFFAX (diffraction of faulted crystals). DIFFAX uses the recursion relationship of the wave function in crystals to simulate planar faults.[19] DIFFAX was used to simulate the first 15 Bragg angles of face-centered cubic crystals with extrinsic and intrinsic stacking faults and twins with probabilities up to 25%. Over 15,000 subreflections due to planar faults were analyzed. It was found that they fit either a delta function or a Lorentzian function. The FWHM and the shift of the subreflections were dependent on the hkl indices and the planar fault probability. The probability followed a fifth order polynomial. Using a data table of the fifth order polynomials for each hkl indices eCWMP is capable of determining the fault probability.[20]

The eCMWP fitting routine simultaneously analyzes the whole profile instead of individual peaks. For a cubic lattice it provides the following parameters: i) the mean size, ii) standard deviation, with which one can find $\langle x \rangle_{area}$, the area weighted mean crystallite size, iii) β the fault or twin probability, iv) ρ the dislocation density, and v) q, a parameter that is dependent on the dislocation type, screw or edge.

When analyzing the X-ray diffraction data the following protocol was followed:

First the FWHM of the *111* peak was found and a rough estimate of the crystallite size was calculated using the Scherrer method. A general trend in the crystallite sizes could be inferred from this data.

Next, the intensity as a function of the length of the diffraction vector K was plotted, where the diffraction vector is defined as:

$$\mathrm{K} = \frac{2\sin\theta}{\lambda} \tag{2-19}$$

where θ is the angle of incidence and λ is the wavelength of the X-ray radiation. The FWHM of the diffraction vectors was plotted versus the Miller indices; this is called a Williamson-Hall plot, see Figure 16. By analyzing the trend in the FWHM values in the Williamson-Hall plot the prominent defects causing line broadening can be determined. Because of the anisotropic strain field of the dislocations and the elastic constants of crystals if dislocations are a prominent cause of line broadening, there will be a non-monotonic increase in the Williamson-Hall plot.[18] As discussed above there is relationship between the average contrast factor and specific *hkl* values, see Equation (2-18). There is

also a relationship between the average strain and the average contrast factor, see Equation (2-16). It is easy to see that there will be an order-dependence in FWHM values due to dislocations. Because planar faults lie in the *111* plane the FWHM values of harmonic pairs of planes, e.g. the *111*/*222* planes, will be order-independent if planar faults play a prominent role in line broadening. For example, in Figure 16 the harmonic pairs *111*/*222* and *200*/*400* have very similar values. It was therefore supposed that this sample had a large percent of planar defects. This was later verified using the eCWMP method. Hence, by careful analysis of the Williamson-Hall plots the defects present in the crystals can be inferred.

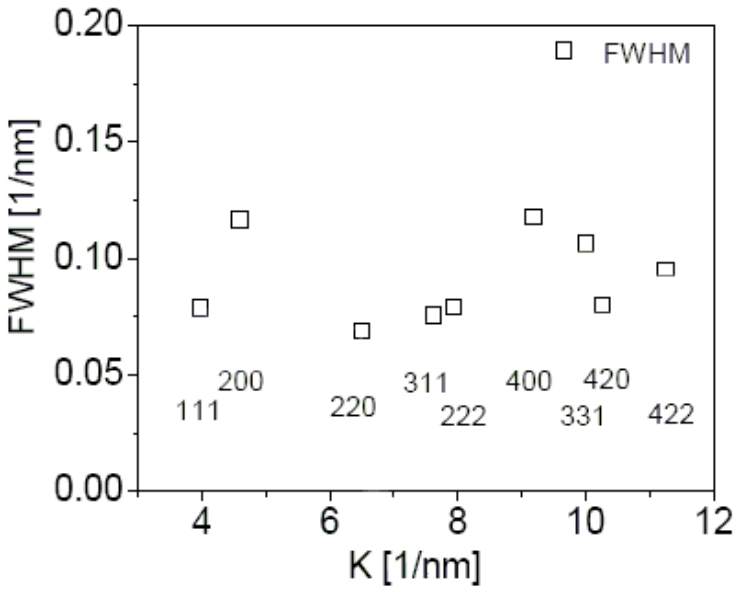

Figure 16 – The Williamson-Hall plot of the SiC compact sintered at 2.0 GPa and 1800 ^{o}C.

Finally the X-ray diffraction data were analyzed using the eCMWP method. First the background is eliminated using cubic splines. Next instrumental broadening is accounted for by taking a Fourier transform of LaB_6 powder diffraction pattern. LaB_6 is a

large crystal powder with very few defects, therefore any broadening will be due to instrumental effects. Next the X-ray data minus the background data and instrumental effects is fit assuming twins, intrinsic stacking faults, and extrinsic stacking faults. The eCMWP procedure is performed many times to verify that the parameters always converge to the same values. By comparing the total sum of residuals when twins, intrinsic stacking faults, and extrinsic stacking faults are assumed the predominate planar fault can be found. The numerical results of the eCMWP fitting are also compared to the anticipated results found from the Scherrer method and by looking at the Williamson-Hall plots to verify the results.

For the nano-sized diamond composites the alp (apparent lattice parameter) method was also used to measure stress in the core and shell of the diamond and SiC phase. Analysis of the peak location in nano-sized crystals can yield useful information. Recall that Bragg's equation, Equation (2-1), equates the location of the peak with the planar spacing of the crystal. Since the powder method was used and this method simultaneously records several crystals and each crystal consists of numerous planes, if the average planar spacing is changed due to strain, then the Bragg angle corresponding to that *hkl* plane would also change. By analyzing the peak positions it is possible to measure changes in the planar spacing and thus measure if the crystals are being contracted or expanded.

Recall from Chapter I that planar faults introduce stacking sequences which resemble the hexagonal structure.[20-22] The cubic structure can be defined by one parameter, the lattice constant a_{cubic}, the hexagonal structure, however, requires two lattice

parameters. There is an in-plane lattice parameter, a_{trig}, and the parameter which is normal to the layer plane c_{trig}. The introduction of the stacking fault will also elongate the "cubic" unit cell in the <111> direction. The cell actually can no longer be considered a cubic and its elongation, or lattice parameter, is going to be a ratio of c_{trig} / a_{trig}. For a cubic crystal $c_{trig} = a_{cubic}\sqrt{3}$ and $a_{trig} = a_{cubic} / \sqrt{2}$, where a_{cubic} is the lattice parameter of a cubic. Since there are three plane spacings between opposite corners in the <111> direction we can define a new variable, $c_{0,trig} = c_{trig} / 3 = a_{cubic} / \sqrt{3}$. In a cubic the ratio of $c_{0,trig}$ to a_{trig} is $\sqrt{2/3} \approx 0.8165$.[23] An increase in this value would indicate that there is elongation due to strain. An increase in the planar faults will result in more stacking sequences which resemble the hexagonal structure.[24,25] And as such the lattice parameter will change depending on the population of planar faults. By finding the Bragg angles we are no longer finding the lattice parameter of a cubic unit cell but the average lattice value, which we renamed the apparent lattice value. With this information it is possible to measure the strain in crystals due to planar faults.

In addition to finding the elongation due to changes in the $c_{0,trig}$ to a_{trig} ratio, changes in the volume of the lattice can also be calculated. Using the $c_{0,trig}$ and a_{trig} values it is possible to measure the volume of the unit cell. Corresponding to this volume there is a cube that has the same volume and a cubic length of EClp (equivalent cubic lattice parameter). By comparing the EClp values of the composites and of the raw powders we can find if the lattices are compressed or stretched due to strain. This is the alp method the results of which will be discussed more in Chapters IV and V.

CHAPTER III. EXPERIMENTAL FRAMEWORK

3.1. High Pressure High Temperature Sintering

Diamond and SiC compacts and diamond-SiC composites are created under high pressure high temperature (HPHT) conditions using a toroidal system or a high pressure piston system, depending on the pressures required. For pressures above 3 GPa the toroidal system must be used to maximize the life span of the pressure vessel used in the piston system. For pressures below 3 GPa either system can be used, depending on the required temperature and the preference of the user. The HPHT protocol is the same for both systems. First the pressure is increased until the desired set point is reached. While the system is under pressure the temperature is rapidly increased by applying a current to a graphite cylinder till the desired sintering temperature and time is reached. Next the system is allowed to cool, while still under pressure. Finally the pressure is slowly released.

In both systems pressure calibration curves were created beforehand by measuring known pressure induced phase transitions of Bi, Tl, PbSe, and PbTe. Pressure calibrations were originally performed over five years ago. Therefore, the pressure calibrations had to be rerun to verify these values. A sample was prepared as in Figure 17, with the sample powder being Pb. The pressure was slowly increased at room temperature and the resistivity of the system was monitored using a Labview program written by C. Pantea. As Pb goes through phase transformations its restivity also changes. By comparing the applied

pressure that resulted in phase transition we were able to verify the load pressure. This procedure was repeated for other compounds. It is estimated that the pressures are accurate to within 10%.

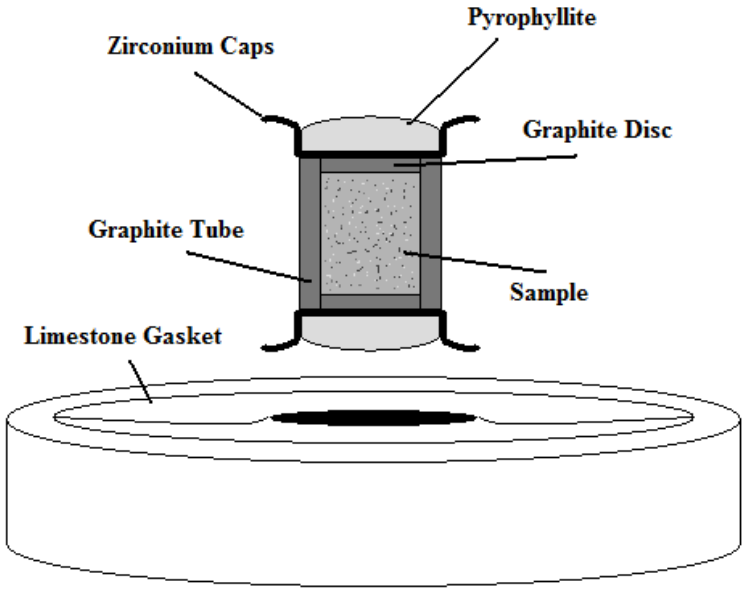

Figure 17 – The limestone gasket and graphite furnace used in the toroidal system.

The high pressure piston system allows HPHT experiments to be run with a W5%Re-W20%Re thermocouple to measure the temperature in situ, see Figure 18. While the experiment is being run the temperature can precisely be controlled by varying the output power based on the thermocouple reading. Although the graphite tube used in the piston system is 32 mm, the sample size is usually limited to 2 – 3 mm. There is a very large temperature gradient in the graphite tube. For more uniform results it is best to limit the size of the sample and center it in the tube.

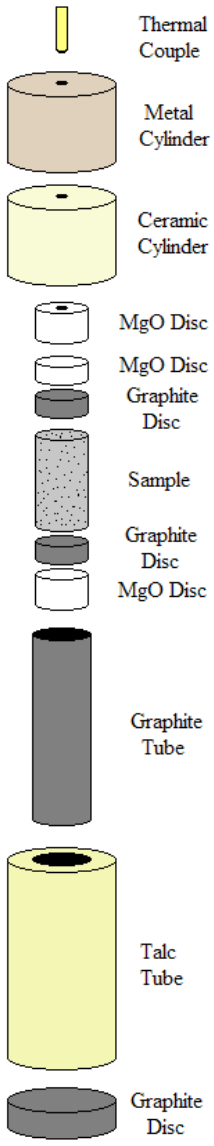

Figure 18 – The sample preparation for the high pressure piston system.

It is very difficult and costly to attach a thermocouple to the toroidal system. Therefore, beforehand a W5%Re-W20%Re thermocouple is used to create temperature curves for the toroidal system using various output powers at different temperatures. These curves are used to determine the required output power for each HPHT experiment that uses the toroidal system. Temperature curves were verified by measuring the melting

temperature of Cu and Si at set pressures. Small grains of Cu or Si were added to nano-diamond powders and the output power was applied. By examining the samples post sintering it was obvious if the Cu or Si melted. The measured output power of the melting point of Cu or Si was then compared to the temperature curve for the same pressure and to known values to verify the temperature calibration. It is estimated that the temperature measurements were accurate to within 50 ^{o}C.

In the toroidal system there are two identical anvils with toroidal grooves. A graphite tube which acts like a furnace is placed in a limestone gasket with contours that match the grooves of the toroidal anvils. The powder to be sintered is placed in the middle of the graphite furnace with graphite discs and pyrophyllite or MgO caps on both ends, see Figure 17. A pallet is often created from the powders to be sintered using a hand press and a pressure of 1000 psi. This reduces the volume of the powders and allows more material to be sintered. The graphite discs and zirconium caps act as conductors to conduct electricity from the toroidal anvils to the graphite tube. As the pressure is released non-uniform expansion of the holder and the materials inside the holder leads to applied stresses which can lead to the cracking of the sample. Therefore a pressure medium is used on both ends of the sample to make sure the pressure is released uniformly in all directions. When preparing the samples at Texas Christian University, pyrophyllite is used as a pressure medium. Samples made at Unipress used MgO as a pressure medium. Even with the pressure mediums some samples, particularly the compacts, were prone to breaking.

The graphite furnace in the piston system is prepared in a similar manner. The furnace is placed in a water free talc tube, which is placed in a pressure cell and pressure is applied with pistons. It was found that using talc tubes which were not annealed resulted in rapid graphitization. This was speculated to be caused by the presence of water in the tubes. Therefore, beforehand the talc tubes were baked at 900 ^{o}C for 2 hours. Samples were created in: TCU, Fort Worth, Bakul Institute for Superhard Materials of Nas, Kiev, Ukraine, and Unipress, Warsaw, Poland.

3.2. Microscopic Imaging

Surface images of the samples were taken using a scanning electron microscope (SEM). All the SEM images were taken using a JEOL SM-6100. The probe current ranged from 10^{-12} to 10^{-6} A and had a magnification range of 750 to 4500×. Images of thin cross sections were taken using transmission electron microscopes (TEM).

Three TEMs were used to create the images: (a) a Philips CM-20 with an operating voltage of 200 kV, (b) a Philips EM 300 with an operating voltage of 100 kV, and (c) a JEOL JEM 3010 with an operating voltage of 200 keV. Ditabis imaging plates were used to record images from the Philips CM-20 TEM, the EM 300 also used imagining plates, and the JEOL used a Gatan camera. The samples being imaged must be very thin to use the TEM. In order to accomplish this first the samples were mechanically ground and then they were ion milled until perforation took place.

3.3. X-ray Diffraction

X-ray diffraction data were collected using a Philips X'pert powder diffractometer with a Cu anode, a Nonius FR 591 with a Cu anode, and beams X14A and X16C at the National Synchrotron Light Source (NSLS), Brookhaven National Labs (BNL). In each case the incident beam had a larger surface area than the sample and the penetration depth was believed to be the entire depth of the sample.

The Philips X'pert diffractometer has a single crystal Si to allow only K_{α_1} radiation. Because the beam is weak the radiation cannot thoroughly be filtered and a measurable amount of K_{α_2} is present in the diffraction patterns. The diffraction data were taken over 6 to 12 hours. The minimum 2θ step size is 0.01^{o}. The x-ray source has a fixed single slit. K_{α_1} radiation for copper has a wavelength of 1.54 Å. Because of the poor filtering and large 2θ step size the Philips was used primarily for cursory analysis.

The Nonius FR 591 has a rotating anode, which can be better cooled than the Philips. For this reason the beam can be more intense and can be more thoroughly filtered. The presence of K_{α_2} is negligible. A Cu anode was used in the Nonius system, so the wavelength was also 1.54 Å. The dwell times were around 24 hours. Light sensitive imaging plates were placed at a fixed distance in a circle around the sample. The imaging plates were arranged such that the diffraction peaks were centered in the middle of each plate to reduce diffraction data that might be lost due the edge of the plate. The imaging

plates were scanned into a tiff image and the intensities were calculated by integrating the dots in an area so that a traditional looking diffraction pattern could be obtained.

Two beams at the NSLS were used, beam X14A and X16C. Since synchrotron light is a continuous beam LaB_6 was used before hand to calculate the wavelength. Beam X14A had a wavelength of 0.80532 Å. X14A has a $\Delta E/E$ resolution of 2×10^{-4}. The monochromator consisted of two Si(111) crystals. The first crystal was flat and was water cooled. The second crystal conically bent. Before reaching the sample the intensity of the primary beam was measured using an ion chamber. The diffracted beam was then normalized based on the decay of the source. The diffracted beam was reflected by a Ge(111) crystal analyzer before being detected by a NaI scintillation counter. Diffraction measurements were taken at room temperature. The 2θ step size was 0.01^o from the 2θ range of 13^o to 60^o and 0.02^o from 60^o to 126^o. Beam X14A was used to measure the nano-diamond composites.

Beam X16C was used on two separate occasions. On both occasions detailed measurements of LaB_6 were used to calculate the wavelengths. The wavelength of the beam that was used to measure the micron-diamond composites was 0.700385 Å. The wavelength of the beam used to measure the nano-diamond compacts was 0.698914 Å. X16C has a $\Delta E/E$ resolution of 2×10^{-4}. It uses a Siddons channel-cut Si(111) monochromator. A vertical two-circle diffractometer with a Ge(111) analyzer was used to take the diffraction data. Diffraction data were taken at room temperature with 2θ range of 13^o to 75^o and step size of 0.001^o. The average dwell time per step was 1 second. Because

the crystals were much larger than those in the nano-diamond composites it was expected that the peak broadening due to size effects, recall Chapter II, was smaller and difficult to analyze. Therefore the step size had to be much smaller to get the best signal to noise ratio. Accurate measurements of narrow band shapes are critical in the analysis of their broadening.

CHAPTER IV. SILICON CARBIDE

Silicon carbide, SiC, is used as a binding phase in diamond composites. It is a hard substance but has a lower hardness than diamond and can greatly affect the overall mechanical properties of the composites. For this reason it is important to study the crystallite and defect growth mechanisms of pure SiC compacts. SiC is produced in composites when liquid Si reacts with carbon from the diamond crystals. The crystal growth of this SiC is limited to the gaps in-between the diamond crystals and is dependent on the sintering conditions. It is therefore sufficient to study SiC compacts produced from nanocrystalline SiC and not necessary to analyze compacts created from microcrystalline SiC.

4.1. SiC Compacts

SiC compacts were produced from nanocrystalline SiC powder with a nominal grain size of 30 nm. They were sintered at temperatures of 1400, 1600, and 1800 ^{o}C and pressures of 2, 4, and 5.5 GPa. An additional sample was sintered at 1800 ^{o}C and 8 GP. There were a total of 10 samples produced. The 2 GPa samples were produced using a piston-cylinder cell system and the other samples were produced using a toroid high pressure system, both systems are described in Chapter III.

X-ray diffraction analysis was performed on the samples. In the case of pure SiC it was sufficient to use the Philips X'pert powder diffractometer with a Cu anode and the high resolution Nonius with a rotating Cu anode, both described in Chapter III. A typical X-ray diffraction pattern can be seen in Figure 19. One can notice that there are graphite peaks present in each of the diffraction patterns. By comparing the areas under the first diffraction peak of SiC and graphite one can estimate that graphite constitutes between 2 and 5 percent of the compacts volume. The graphite is most likely a residual effect of the graphite furnaces used in the production of the compacts. The graphite can become embedded in the surface during the high pressure production. Even though polishing was performed on the samples it can be difficult to remove all of the graphite without damaging the samples. This observation is not a numerical artifact. The graphite peaks and SiC peaks are sufficiently far apart from each other, therefore there was a negligible overlapping and the analysis gave trustworthy results.

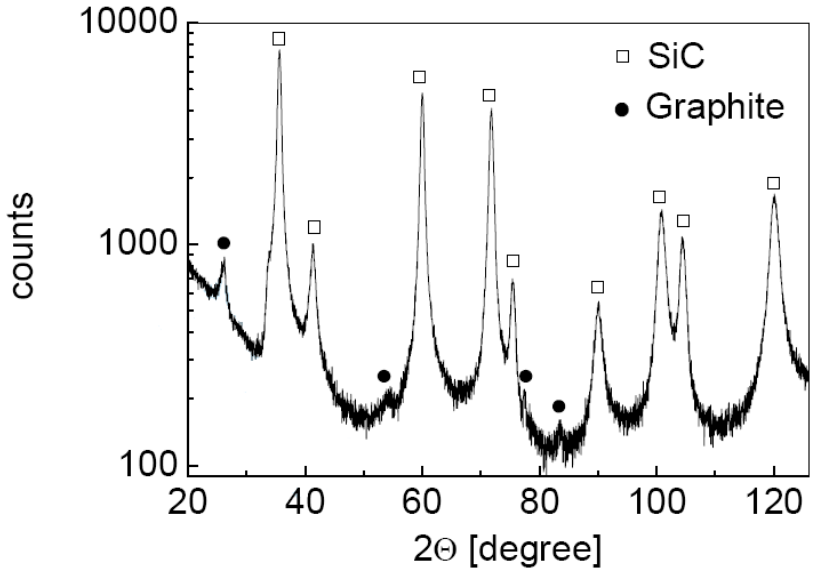

Figure 19 – The X-ray diffraction in logarithmic scale for the nanocrystalline SiC compact sintered at 2 GPa and 1800 ^{o}C.

Observation of the X-ray diffraction patterns also revealed a shoulder to the left of all the SiC *111* peaks, see Figure 20. This satellite peak can be found centered at 2θ = 33.6°. It was suspected that this additional peak was a result of the presence of planar faults in the SiC phase. Theoretical X-ray diffraction patterns were produced using the DIFFaX software.[19] In these simulations 10% intrinsic and extrinsic stacking faults and twins were assumed. In all the simulated patterns a shoulder centered at 2θ = 33.6° was found. A simulated X-ray diffraction pattern assuming twins can be seen in Figure 21.

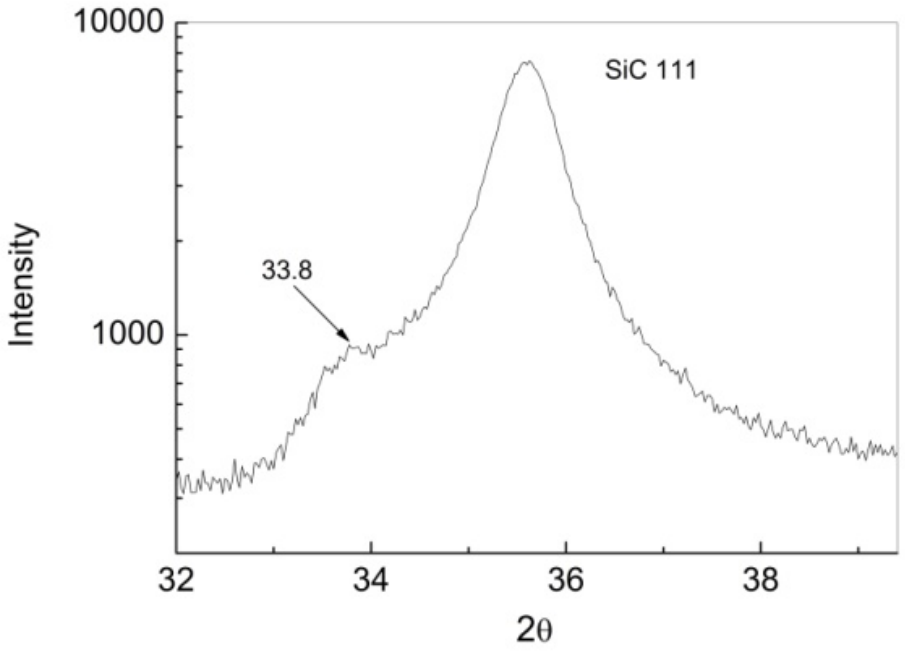

Figure 20 – The X-ray diffraction pattern of the SiC compact sintered at 2 GPa and 1800 °C.

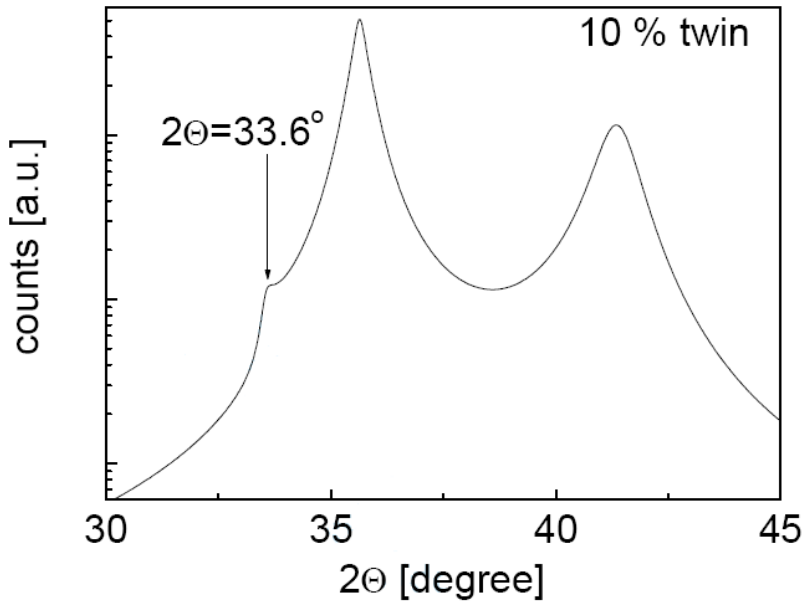

Figure 21 – The calculated X-ray diffraction pattern using DIFFaX assuming 10% twins.

To better determine the prevalent defects present in the microstructure the Williamson-Hall plot from each sample's X-ray diffraction pattern were created, as discussed in Chapter II. The Williamson-Hall plots, followed one of two patterns. In one case the FWHM values between reflection pairs, for example *111*/*222* and *200*/*400*, are order independent, as seen in Figure 16. This would indicate that peak broadening is mainly dependent on small crystallite size and planar faults. This pattern in the Williamson-Hall plots was found in the samples sintered at pressures less than 4 GPa and temperatures less than 1600 ^{o}C. However, in the samples sintered at higher temperatures and pressure there is a strong order-dependence of the FWHM and the Williamson-Hall plot has a pattern more similar to Figure 22.

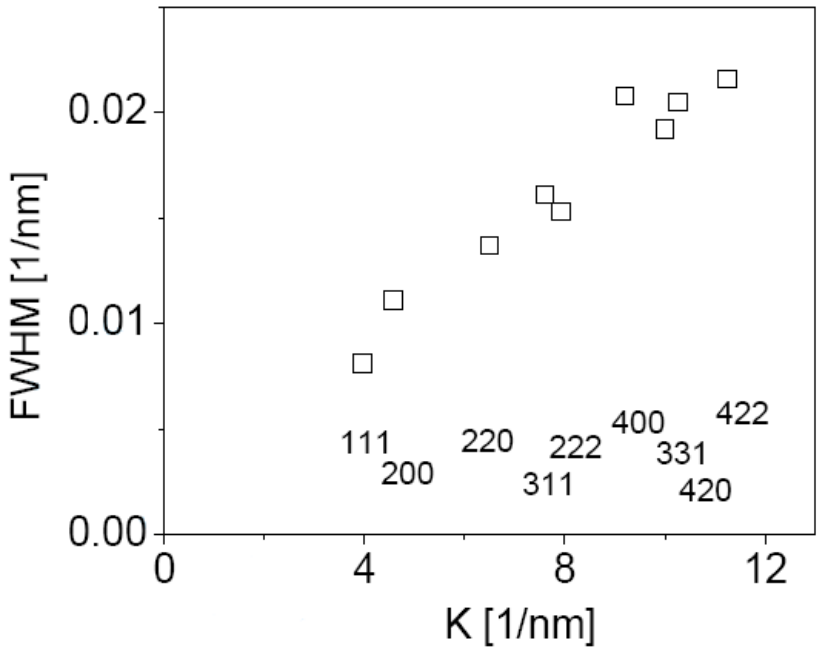

Figure 22 – The Williamson-Hall plot of the SiC compact sintered at 5.5 GPa and 1800 ^{o}C.

Dislocations cause peak breadths to have a dependence on the Miller indices.[18] When dislocations are present the breadth of a peak is smallest for the smallest K value and the Williamson-Hall plot displays a non-monotonic trend with increasing K.[18] As was mentioned in Chapter II, anisotropic strain broadening is caused by anisotropic effects in the crystal, including strain field of the lattice defects and the elastic constants. The broadening due to dislocations will therefore be dependent on the relative orientations of the line and Burgers vectors of the dislocations and the diffraction vector. It has been shown that the average contrast factors, C, considers the effects of the anisotropic contrast of dislocations in a non-textured polycrystalline material. The contrast factors can be calculated numerically based on the dislocations and elastic constants of the crystal. The average value of C for a non-textured pollycrystallite is a fourth order polynomial of the Miller indices, Equation (2-18). It is also known that when anisotropic broadening is

caused by dislocations the FWHM values are dependent on K^2C. The modified Williamson-Hall plot of the FWHM versus K^2C can be seen in Figure 23. There it is evident from the smooth curve that dislocations play a predominate role in the broadening of peaks of the samples sintered at higher pressures and temperatures.

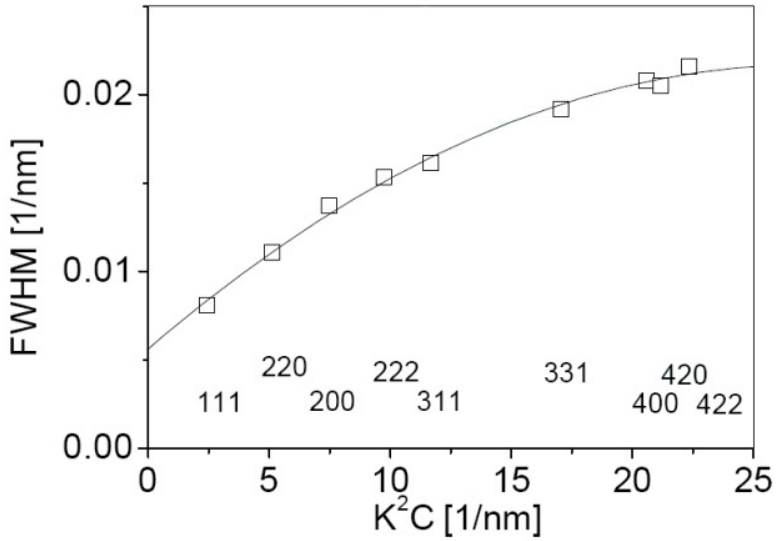

Figure 23 – The modified Williamson-Hall plot of the SiC compact sintered at 5.5 GPa and 1800 ^{o}C.

Since line broadening was caused by dislocations, planar faults and crystallite size, it was best to analyze the X-ray difffraction data using the eCMWP method, an example of the fitting can be found in Figure 24. Analysis was carried out on all of the samples assuming: twins, extrinsic faults, and intrinsic faults. The sum of the residuals was smallest for each of the calculations when twins were assumed. This is consistent with the symmetric nature of the peaks, as opposed asymmetries usually found with intrinsic or extrinsic faults. Hence forth, for the SiC compacts when talking about planar fault probability I will be referring to twins. Table 1 shows the microstructure parameters of

nine of the samples. Please note that dislocations densities less than 10^{13} m^{-2} are not detectable by eCMWP.

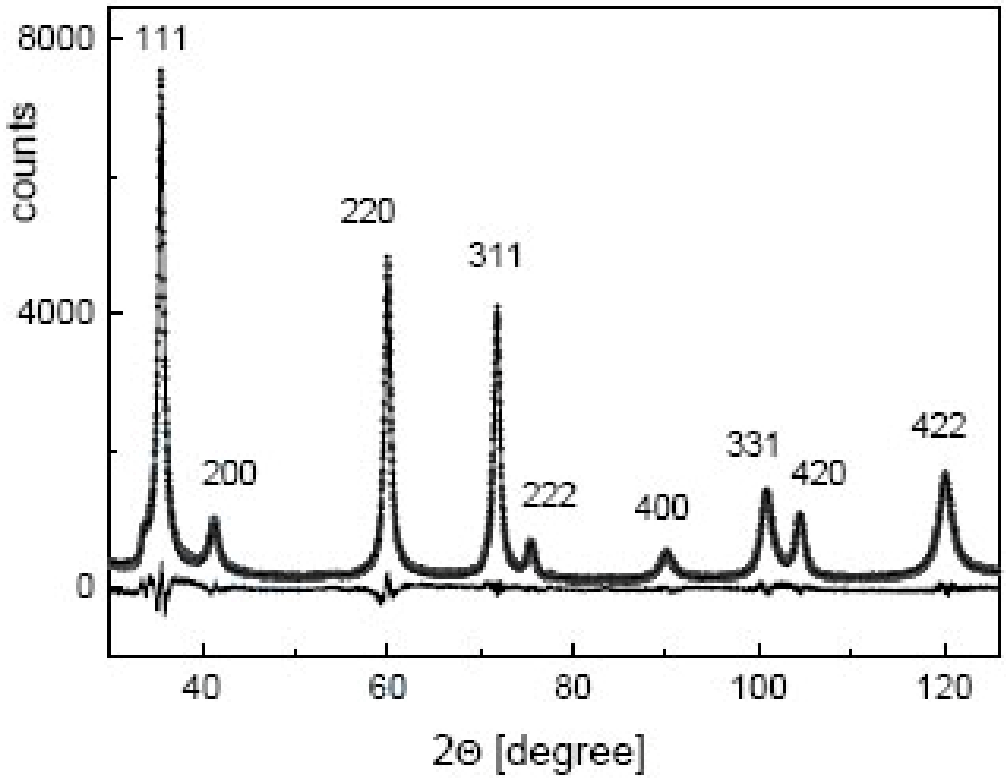

Figure 24 – The eCWMP fitting of the SiC compact sintered at 2 GPa and 1800 ^{o}C. Open circles are the measured pattern, the solid line is the fitted pattern and the line on the bottom is the difference between the two.

Table 1 – The calculated parameters of the microstructure of the SiC compacts for various temperatures and pressures: $\langle x \rangle_{area}$ is the area-weighted mean crystallite size, β is the planar fault probability, and ρ is the dislocation density.

Pressure (GPa)	2	4	5.5
Temperature (^{o}C)			
1400	$\langle x \rangle_{area} = 8.9 \pm 0.8\,\text{nm}$ $\beta = 9.4 \pm 0.9\%$ $\rho < 10^{13}\,\text{m}^{-2}$	$\langle x \rangle_{area} = 15 \pm 1\,\text{nm}$ $\beta = 11 \pm 1\%$ $\rho < 10^{13}\,\text{m}^{-2}$	$\langle x \rangle_{area} = 19 \pm 1\,\text{nm}$ $\beta = 11 \pm 1\%$ $\rho < 10^{13}\,\text{m}^{-2}$
1600	$\langle x \rangle_{area} = 13 \pm 1\,\text{nm}$ $\beta = 11 \pm 1\%$ $\rho < 10^{13}\,\text{m}^{-2}$	$\langle x \rangle_{area} = 16 \pm 1\,\text{nm}$ $\beta = 11 \pm 1\%$ $\rho < 10^{13}\,\text{m}^{-2}$	$\langle x \rangle_{area} = 94 \pm 7\,\text{nm}$ $\beta = 0.20 \pm 0.03\%$ $\rho = 0.40 \pm 0.08 \times 10^{15}\,\text{m}^{-2}$
1800	$\langle x \rangle_{area} = 13 \pm 1\,\text{nm}$ $\beta = 11 \pm 1\%$ $\rho < 10^{13}\,\text{m}^{-2}$	$\langle x \rangle_{area} = 124 \pm 10\,\text{nm}$ $\beta = 0.10 \pm 0.02\%$ $\rho = 0.30 \pm 0.08 \times 10^{15}\,\text{m}^{-2}$	$\langle x \rangle_{area} = 126 \pm 10\,\text{nm}$ $\beta = 0.17 \pm 0.03\%$ $\rho = 0.40 \pm 0.08 \times 10^{15}\,\text{m}^{-2}$

The average grain size increases as a result of sintering. As pressure is held constant there is growth in the average crystallite size as temperature is increased. Likewise as temperature is held constant there is growth in the average crystallite size as pressure is increased. For example, the sample sintered 4 GPa and 1400 ^{o}C had an average crystallite size of 15 nm, the sample sintered at 4 GPa and 1600 ^{o}C had an average crystallite size of 16 nm, and the sample sintered at 4 GPa and 1800 ^{o}C had an average crystallite size of 124 nm.

TEM images of the samples sintered at 1800 ^{o}C and 2 and 5.5 GPa can be found in Figures 25 and 26. The values of the grain sizes observed in the TEM images range from 30 to 100 nm for the 2 GPa sample and 100 to 300 nm for the 5.5 GPa sample. This trend is consistent with the one observed by the X-ray diffraction analysis. Larger values were observed by the TEM but this can be attributed to the fact that x-ray line profile analysis measures the coherently scattering domain size, which is generally smaller than the grain size observable by microscopic methods. This can be caused by low angle disorientations which disrupt the coherence but show only as weak contrast differences in microscopic images. These discrepancies in sizes have previously been reported by Zhu et al.[26]

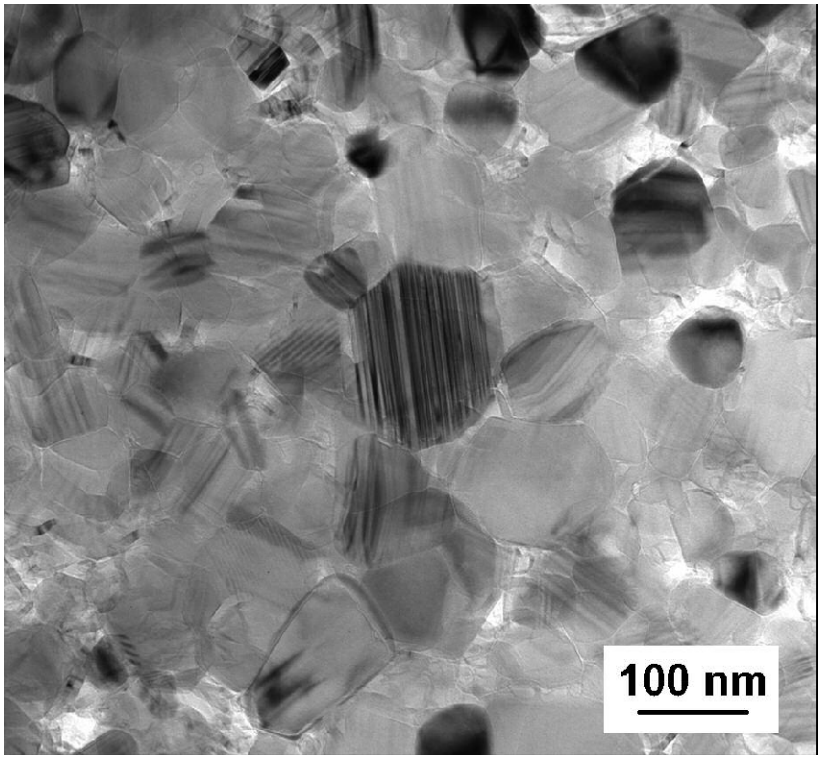

Figure 25 – The TEM image of the SiC compact sintered at 2 GPa and 1800 ^{o}C.

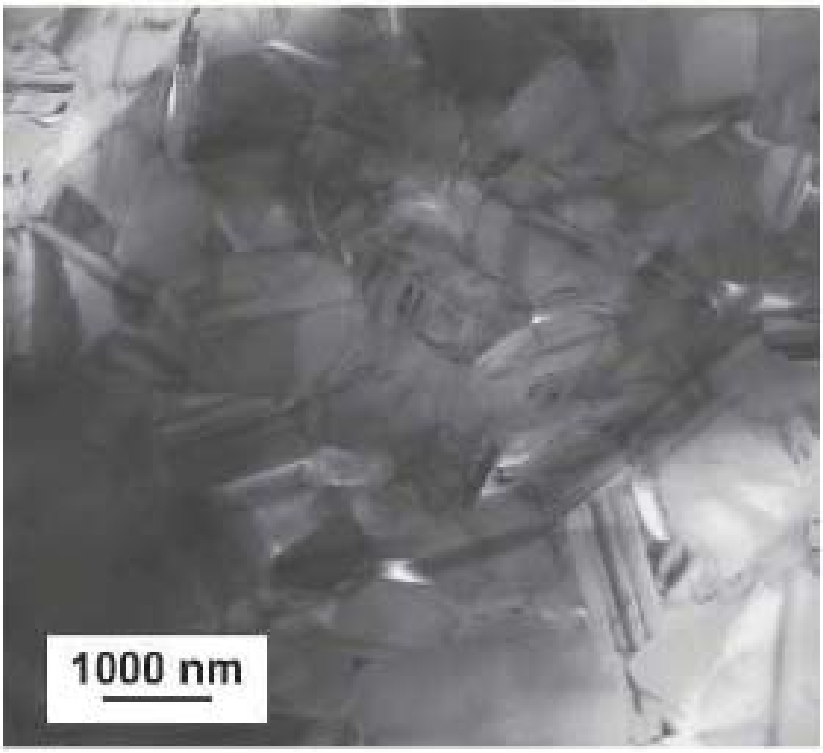

Figure 26 – The TEM image of the SiC compact sintered at 5.5 GPa and 1800 ^{o}C.

At lower pressure and temperature values twins are formed during sintering and the dislocation density is below the detectable range. At temperatures of 1600 and 1800 ^{o}C and above pressures of 5.5 GPa and 4 GPa, respectively, the planar fault probability decreases to less than 0.1% and the dislocation density increases. There is still a presence of planar faults as confirmed by a shoulder of *111* peak. The planar fault population decrease can also be observed in the TEM images, Figures 25 and 26. The distance between faults is 3 to 6 nm and 100 to 200 nm for the 2 GPa and 5.5 GPa samples respectively. Since the distance between planes in the <111> direction is 0.252 nm the planar fault probability can be estimated using the TEM images and they range between 6 and 12 % and 0.1 and 0.2%, for the two samples. This is in good correlation with the X-ray diffraction analysis. Unfortunately the dislocations cannot be detected by TEM. As the

crystallite size increases there is an increase in the dislocation density and a decrease in the planar fault probability. It would appear that at high pressures and temperatures the relatively large crystallite size enables the formation of dislocations during the sintering process. There is also an elimination of planar faults at higher temperature and larger crystallite sizes. This has previously been reported by Koumoto et al.[27]

The specimen prepared at 8 GPa and 1800 ^{o}C had: $\langle x \rangle_{area}$ = 73 ± 8 nm, β = 1.8 ± 0.3%, and ρ = 1.5 ± 0.2 x 10^{15} m^{-2}. The crystallite size decreased compared to the sample sintered at 5.5 GPa and the same temperature, while the dislocation density and planar fault probability increased. Again the TEM images for this sample, see Figure 27, are in correlation with these results.

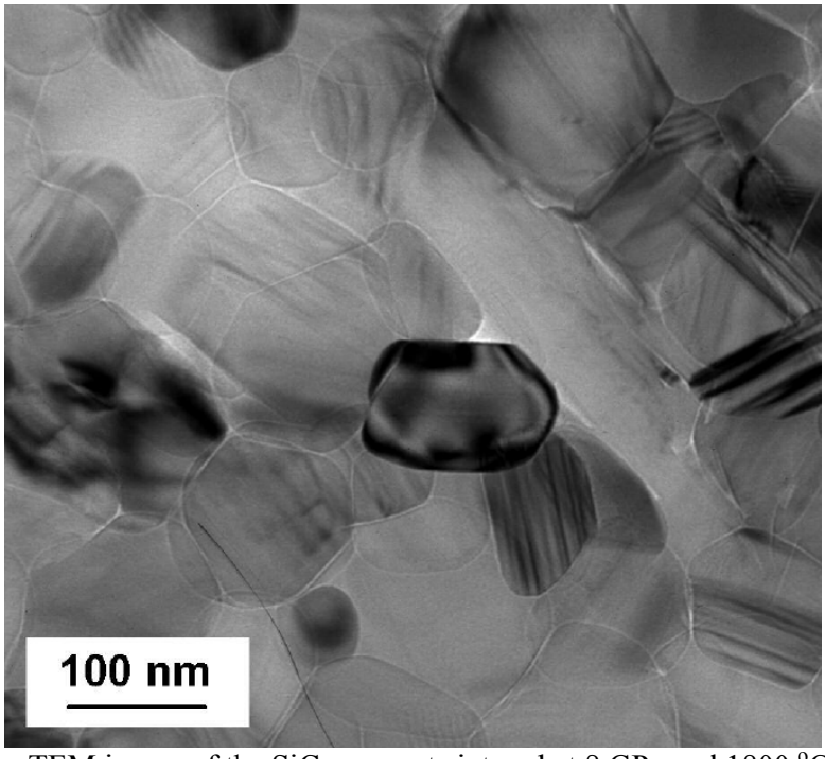

Figure 27– The TEM image of the SiC compact sintered at 8 GPa and 1800 ^{o}C.

4.2. SiC in Diamond-SiC Composites

Next the SiC phase from diamond-SiC composites was analyzed. Two sets of composites were sintered, one using diamond powders with initial grain size of 0 to 50 nm and the other using diamond powder with an initial size of 50-70 μm. Both sets of samples used silicon powder with a nominal grain size of 30 nm.

4.2.1. SiC in Nano-Diamond-SiC Composites

The samples sintered using the nano-sized diamond powder were sintered at a pressure of 8 GPa and temperatures of 1820, 1975, 2190 and 2320 ^{o}C. The diamond powder had an initial size of 0 – 50 nm and the Si powder had a nominal grain size of 30 nm. The diamond to Si powder had a weight ratio of 7:3. Usually in the production of diamond-SiC composites the percent of Si by weight is around 10 – 15%. However, since it is important to study the microstructure of the SiC phase, the weaker of the two phases, we wanted to have strong SiC peaks and used a higher concentration of Si.

The liquid infiltration method usually dictates that inside the sample holder, see Figure 17, a layer of Si powder is placed on top of the diamond layer. As the pressure and temperature are increased the strong capillary forces drive the liquid Si into the pores between the diamonds. There the Si reacts with carbon and forms a SiC matrix. When this procedure was followed using the nano-diamond powder it was found that the Si did not

completely infiltrate the diamond powder. Therefore a new procedure was introduced. First the powders were combined and added to ethyl alcohol and mixed using an ultrasonic mixer. The mixture was then placed inside of a cylinder and mechanically rotated for 2 days. The mixed powder was then added to the sample holder. And the usual HPHT protocol was followed. Even with the mixing there were scattered regions within the composites which consisted of conglomerates of predominately diamond, see Figure 28.

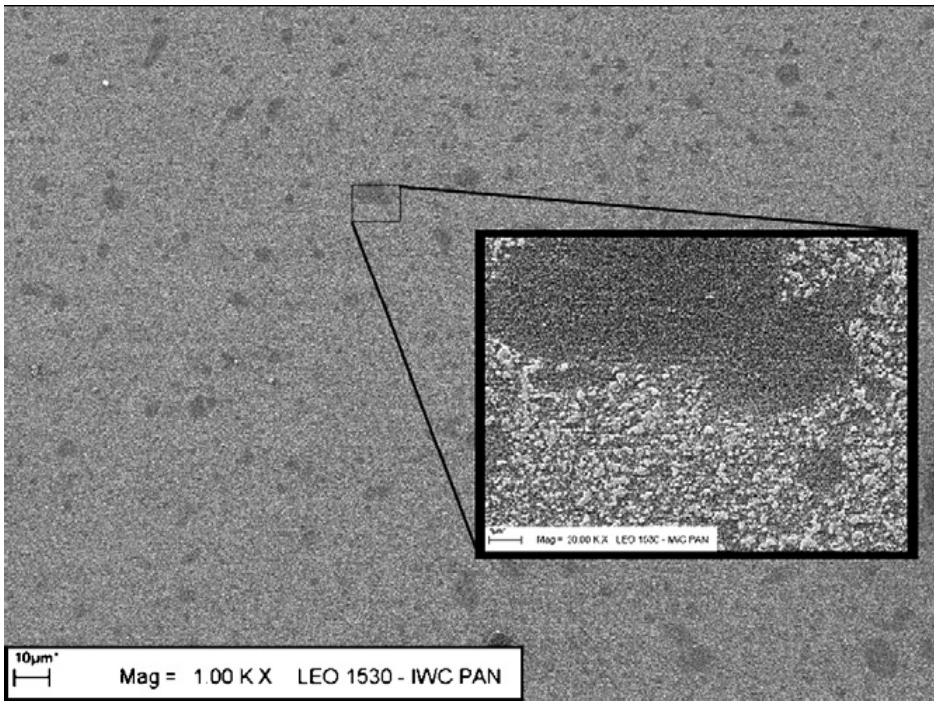

Figure 28 – SEM image of the nano-diamond-SiC composite sintered at 1820 ^{o}C. The sample is not completely uniform. Self-aggregation of nano-diamond, the white areas, is very difficult to avoid even with long mixing times.

X-ray diffraction data was taken using beam X14A at the NSLS, BNL. The typical X-ray diffraction pattern can be seen in Figure 29. It is important to note that the only peaks present are diamond and cubic SiC. The lack of Si indicates that the sintering process was complete and the lack of graphite peaks indicates that the sintering process

took place at temperatures and pressures where diamond is the stable form of graphite. One can also notice a shoulder to the left of all of the SiC *111* peaks, see Figure 30. As mentioned above this shoulder indicates a presence of planar faults in the SiC phase. In Figures 29 and 30 it is apparent that the shoulder of the sample sintered at 1820 ^{o}C is more pronounced than that of the 2320 ^{o}C sample. This would seem to indicate a higher percentage of planar faults in the 1820 ^{o}C sample. One can also notice in those figures that the broadening is greater in the sample sintered at 1820 ^{o}C. This would indicate that the crystallite size is smaller for this sample.

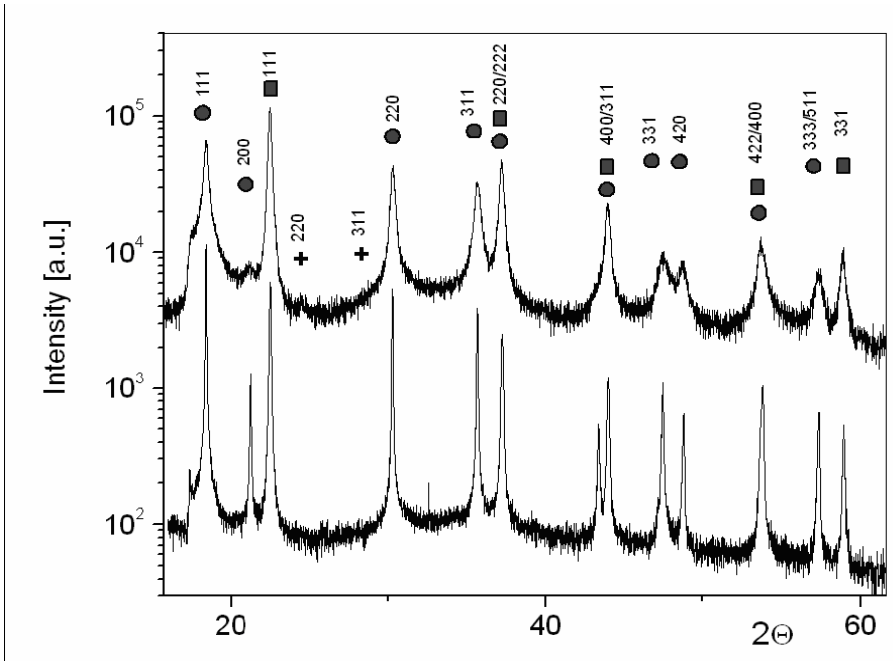

Figure 29 – The X-ray diffractograms for the nano-diamond-SiC composite sintered at 8 GPa and 1820 ^{o}C, top, and 2320 ^{o}C, bottom. The circles are the SiC peaks, squares are the diamond peaks, and the pluses are where Si peaks would be.

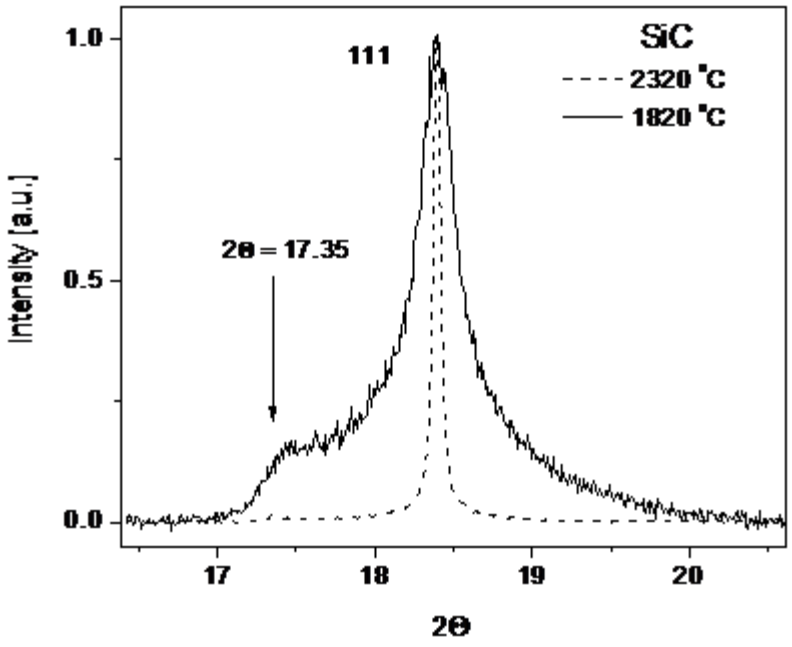

Figure 30 – The *111* peak of the SiC for the nano-diamond-SiC composites sintered at 8 GPa and 1820 and 2320 ^{o}C.

One can compare the Williamson-Hall plot of these samples in Figure 31 to those in Figures 16 and 22. The Williamson-Hall plot of the 2190 ^{o}C lies in-between the 1975 and 2320 ^{o}C samples. The Williamson-Hall plot in Figure 31 has a non-monotonic increase similar to one found in Figure 22. This indicates that line profile broadening is due to dislocations in addition to planar faults and crystallite size. One can also notice that the FWHM values of 1820 ^{o}C sample, Figure 31, and the SiC compact sintered at 2 GPa and 1800 ^{o}C, Figure 16, are much larger than the other FWHM values found in Figure 22. This is primarily due to the broadening due to crystallite size. The samples with the larger FWHM values will have smaller grain sizes due to fewer crystal planes destructively interfering with each other near the Bragg angle.

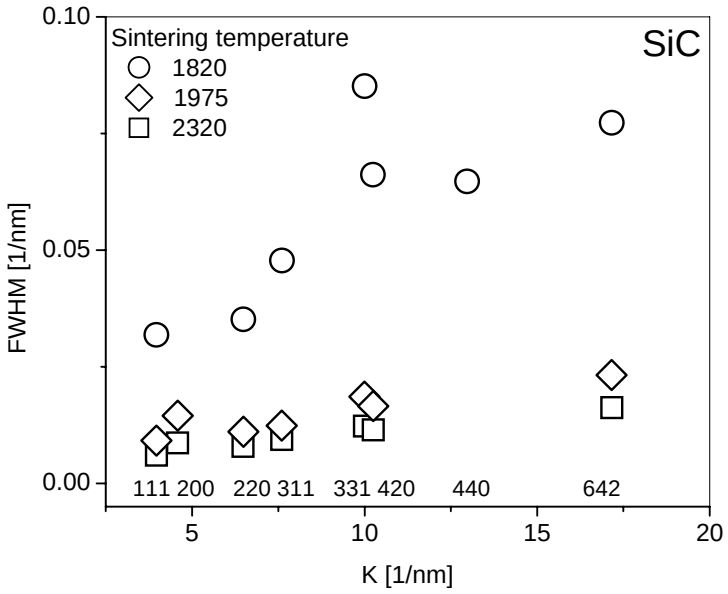

Figure 31 – The Williamson-Hall plot of SiC phase in the nano-diamond-SiC composites.

Since broadening is due to crystallite size, dislocations, and planar faults the eCMWP method was used to estimate the microstructure properties. The values calculated using the eCMWP fitting procedure for the SiC in the nano-sized diamond composites can be found in Table 2. The eCMWP fitting procedure was run assuming intrinsic and extrinsic faults and twins. The sum of the residuals was least when twins were assumed. All planar fault values are given assuming twins. With growing sintering temperature the weighted average crystallite size increases and the planar fault probability decreases. This trend was observed in the SiC compacts. The average crystallite size for the 1820 ^{o}C sample was the smallest, which coincides with the expected results by comparing the FWHM values. The presence of twins was observed in the TEM images, see Figure 32. The tendency of twins to be less prevalent in the sample sintered at higher temperatures was also observed. Unfortunately, since the diamond is harder than SiC, the SiC was

selectively ion milled during preparation for the TEM images. This left only small SiC crystals sandwiched between diamonds. Therefore the size dependence could not be verified. The dislocation density was found to decrease and then increase as sintering temperature increases.

Table 2 – The calculated parameters of the microstructure of SiC in nano-diamond-SiC composites sintered at 8 GP and various temperatures. $\langle x \rangle_{area}$ is the area-weighted mean crystallite size, β is the planar fault probability, and ρ is the dislocation density.

Temperature (^{o}C)	
1820	$\langle \mathrm{x} \rangle_{\mathrm{area}} = 24 \pm 2\mathrm{nm}$ $\beta = 16 \pm 4\%$ $\rho = 3.8 \pm 1 \times 10^{15}\,\mathrm{m}^{-2}$
1975	$\langle \mathrm{x} \rangle_{\mathrm{area}} = 37 \pm 3\mathrm{nm}$ $\beta = 14 \pm 4\%$ $\rho = 2.6 \pm 1 \times 10^{15}\,\mathrm{m}^{-2}$
2190	$\langle \mathrm{x} \rangle_{\mathrm{area}} = 86 \pm 5\mathrm{nm}$ $\beta = 3.8 \pm 1\%$ $\rho = 0.3 \pm 0.1 \times 10^{15}\,\mathrm{m}^{-2}$
2320	$\langle \mathrm{x} \rangle_{\mathrm{area}} = 138 \pm 2\mathrm{nm}$ $\beta = 1.7 \pm 0.5\%$ $\rho = 0.5 \pm 0.1 \times 10^{15}\,\mathrm{m}^{-2}$

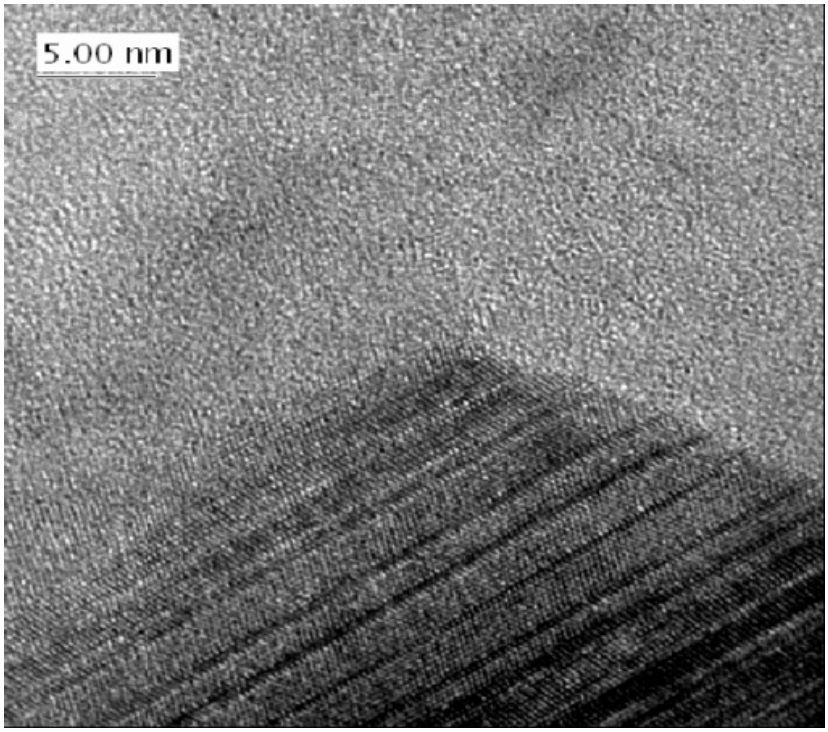

Figure 32 – High resolution transmission electron microscopic image of the nano-diamond-SiC composite sintered at 8 GPa and 1820 ^{o}C. The darker area is SiC and twins are clearly present.

Previous articles have shown an increase in dislocation densities as sintering temperature increases.[28-31] In those research articles a maximum was found at 1800 ^{o}C. In these nano-sized diamond-SiC composites all the sintering temperatures were always above 1800 ^{o}C. This would indicate that at higher temperatures recovery and or recrystallization occurs. This in addition to previous results indicates that at higher temperatures SiC is less brittle than at lower temperatures and plastic deformation can occur.

The bonding of the materials investigated here are mainly of covalent type. The materials are brittle ceramics and plastic deformations are practically absent. Defects in the crystal structure, whether from planar faults or dislocations, affect the interatomic distances and the chemical strengths of the bonds.

The core-shell model of the SiC phase in these nano-sized diamond composites was measured using the alp method, which was discussed in Chapter II. Differences in the grain's structure to that of the core's structure result in changes in the lattice parameters compared to a perfect cubic crystals. Recall that in a cubic crystal $c_{0,trig} / a_{trig} = \sqrt{2/3} \approx 0.8165$. The alp method was applied to a untreated SiC powder and the measured EClp value was 4.356 Å. By modeling the difference in these lattice parameters we were able to determine changes in atomic distance in atoms near the surface or the shell and those in the core of the crystals.

The results of the alp method can be found in Table 3. In the SiC in the samples sintered at the lowest temperature the core's EClp has a larger volume than the SiC powder. As the sintering temperature increases the core's EClp becomes compressed. Eventually the volume is smaller than that of the powder. The interatomic distances of the atoms in the shell are smaller than those in the core for SiC for the sample sintered at 1820 and 1975 ^{o}C. However this trend reverses for the samples sintered at 2320 ^{o}C. The SiC appears to have no shell in the sample sintered at 2190 ^{o}C. This lack of a shell would likely indicate there is no detectable difference in core and shell distances.

Table 3 – Parameters found from the alp method of the SiC in the nano-diamond-SiC composites. $V_{unit\ cell}$ is the volume of the unit trigonal lattice, s_o is the thickness of the surface shell, and $\Delta r/r$ is the relative change in the interatomic distances in the surface shell.

Temperature (^{o}C)	a_{trig} (Å)	$c_{0,trig}$ (Å)	$c_{0,trig} / a_{trig}$	$V_{unit\ cell}$ (Å^3)	EClp (Å)	s_0 (Å)	$\Delta r / r$ (%)
1820	3.077	2.528	0.8214	82.90	4.360	3	-6
1975	3.078	2.523	0.8198	82.81	4.359	3	-2
2190	3.082	2.517	0.8173	82.73	4.357	…	…
2320	3.077	2.512	0.8173	82.51	4.353	5	+6

The core-shell model was also able to show a trend in the planar fault probability. By comparing the measured $c_{0,trig} / a_{trig}$ to that of a cubic crystal it is apparent that the planar fault probability decreased as sintering temperature increased which corresponds to the eCMWP data. It is important to note that the alp method does not explore the band shape and therefore cannot give a quantitative analysis of the planar fault probability.

4.2.2. SiC in Micron-Diamond-SiC Composites

Analysis was also performed on the SiC phase of samples sintered using micron-sized diamonds. Samples were sintered using diamond powder with an initial grain size of 50-70 μm and Si powder with a nominal grain size of 30 nm. These powders were not mixed before sintering. The samples were sintered at 10 GPa and 1600, 1800, and 2000 ^{o}C.

X-ray diffraction analysis was performed for these samples using the x-ray source of beam X16C from the NSLS, BNL. There was no evidence of graphite or other phases besides SiC or diamond in the X-ray diffraction patterns. Like the previous SiC samples there was a shoulder found to the left of the SiC *111* peak. A Williamson-Hall plot of SiC had order dependence, see Figure 33. The pattern is similar to ones found in Figures 12 and 31. This order-dependence indicates that in addition to stacking faults and crystallite size, dislocations play a role in the line broadening of the SiC X-ray diffraction patterns. Since there was a presence of stacking faults and dislocations, the X-ray diffraction data

were analyzed using the eCMWP method. eCMWP analysis was simultaneously performed on ten SiC peaks. The results of the analysis can be found in Table 4. The fitting was done assuming intrinsic and extrinsic stacking faults and twins. The sum of the residuals was a minimum when twins were assumed. As with all the samples the planar fault probability decreased with an increase in sintering temperature.

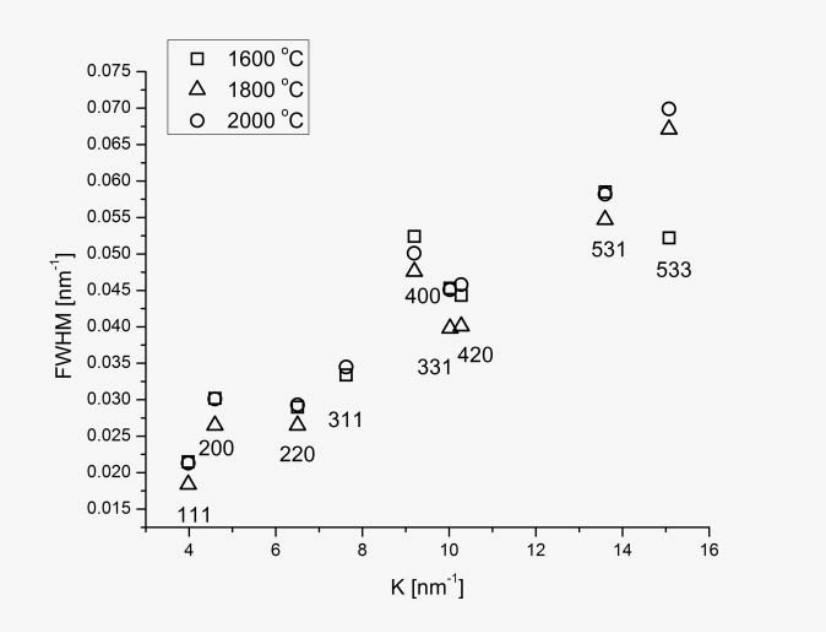

Figure 33 – The Williamson-Hall plot of the SiC phase of the micron-diamond-SiC composite sintered at 10 GPa.

The dislocation density increases as the sintering temperature increases. This trend was found to be the same with the SiC compacts and in other research.[28-31] However, we found at 8 GPa and temperatures of 1820 to 2190 °C the dislocation density decreased. It was supposed that at lower temperatures the SiC phase behaves in a more brittle manner and dislocations can form. However at higher temperatures it is more plastic and

recrystallization or recovery can occur. These results would indicate that at higher pressures even higher temperatures are required for plasticity to occur.

Table 4 – The calculated parameters of the microstructure of the SiC in the micron-diamond-SiC composites sintered at 10 GPa and various temperatures: $\langle x \rangle_{area}$ is the area-weighted mean crystallite size, β is the planar fault probability, and ρ is the dislocation density.

Temperature (^{o}C)	
1600	$\langle x \rangle_{area} = 110 \pm 10\text{nm}$ $\beta = 2.9 \pm 0.1\%$ $\rho = 0.65 \pm 0.05 \times 10^{15}\,\text{m}^{-2}$
1800	$\langle x \rangle_{area} = 100 \pm 10\text{nm}$ $\beta = 1.7 \pm 0.1\%$ $\rho = 0.57 \pm 0.05 \times 10^{15}\,\text{m}^{-2}$
2000	$\langle x \rangle_{area} = 75 \pm 8\text{nm}$ $\beta = 2.0 \pm 0.1\%$ $\rho = 0.63 \pm 0.05 \times 10^{15}\,\text{m}^{-2}$

The results from the SiC compacts led us to hypothesize that the crystallite size may increase due to diffusion of mass from the outer layers of neighboring grains. The presence of partially disordered structures near the grain boundary has been postulated by Keblinski et al.[32] and detected by Yakamoto et al.[33] and Liao et al.[34] These partially disordered structures may allow the diffusion of mass leading to grain growth. It is also possible that increased pressure led to ordering of amorphous or partially disordered phases. In the diffusion process there are two competing factors, temperature, which increases atom mobility and pressure which decreases it. In the nano-diamond sized composite samples there was a much higher temperature which may have led to the increase in the crystallite sizes. In the micron-sized diamond composites the pressure was much higher and the

temperatures were lower. An increase in pressure usually decreases the mobility, however increased elastic shear strains at the contact surfaces may induce the grain growth in the samples sintered at pressures less than 8 GPa. However, at 8 GPa the decrease in mobility due to an increase pressure and increase in elastic shear is balanced with the increase in mobility due to higher temperatures such that grain growth is limited. This may be why there is a decrease in crystallite size as temperature increases. The increase in temperature just increased the expansion of the diamond crystals resulting in more localized pressures. And a high enough temperature needed to overcome the reduced mobility of atoms due to pressure was not reached.

CHAPTER V. DIAMOND

Because of their exceptional hardness and wear resistance diamonds are ideal for industrial applications. However, they have low fracture toughness particularly along certain facets. The use of large diamonds would require careful alignment of the face being used. The use of randomly oriented diamond powders to form composites and compacts is one way to avoid this difficulty. In addition, large diamonds are quite costly. However diamond powders can be manmade and are relatively cheap. The overall physical qualities of the compacts and composites are going to be dependent on the microstructure of the crystals that comprise them. It is therefore important to study the microstructure of diamonds in composites and compacts after various sintering conditions.

5.1. Diamond Compacts

Because of their more isomorphic shapes and large surface energy, nano-diamond powders can be more attractive than micron-diamond powders for use in industrial applications. Diamonds will go through phase transformations into graphite at high temperatures and under non-hydrostatic conditions or when deformations are introduced.[36,37] Deformations can be introduced from non-hydrostatic conditions. During the high pressure phase of the production of diamond compacts from micron-diamond powders the diamond crystals are pushed into each other. This causes small pieces of the crystals to shear off. These small crystals then can fill the voids between the larger

crystals. This creates an environment more conducive to hydrostatic conditions.[38] Qian et al. also found that nano-diamond powders graphitize more rapidly than microcrystalline diamonds.[37] Also nanodiamond powders are surrounded by an amorphous carbon layer.[37,39] This layer transforms into graphite at temperatures above 1200 ^{o}C. This was discovered by Palosz, et al.[39] who used neutron diffraction techniques and Qian, et al.[37] who used high resolution TEM.

In order to reduce graphitization diamond compacts sintered at high temperatures must also be sintered at high pressures and the pressures must be hydrostatic. Experimentally it was found that the nano-diamonds resist the breaking under high pressures and would therefore be less likely to be in hydrostatic conditions. This was found by creating a sample compact of nano-diamonds at 8 GPa and room temperature. After compacting the porosity was measured and found to be 55%. It is believed that the resistance to breaking is caused by the large surface energy. Since the nano-diamonds resisted the breaking they were less likely to be in hydrostatic conditions and more likely to graphitize. For that reason and because of the amorphous carbon layer and the more rapid graphitization times, sintering times for nano diamonds were kept very short in hopes of avoiding graphitization.

The diamond compacts were sintered under HPHT conditions using monocrystalline diamond powder with an average grain size of 25 nm. The sintering pressure was 8 GPa and was achieved using a toroidal system. The output power to control the temperature was very high but the sintering times were very short, as to reduce

graphitization. Traditionally sintering times are the times that the sample is kept at the desired temperature. However, for these experiments the sintering time is the total time that power was applied. Given sufficient time, about 15 seconds, the temperature reached would be 2370 ^{o}C. Since the sintering times were below 15 seconds that temperature was never reached. The sintering times were 5, 7, 9, and 11 seconds and the final temperatures reached were 1975, 2190, 2320, and 2390 ^{o}C, respectively. Once the final temperature was reached the output power was turned off and the samples were allowed to cool under pressure. Very little difference was found in the 5 and 7 second samples and the 9 and 11 second samples, so I will only discuss the 5 and 11 second samples.

The temperatures followed the curve found in Figure 34. The temperature curve was found using a W5%Re-W20%Re thermocouple and verified by measuring the melting temperature of Si and Cu. Si or Cu powders were added to the diamond powder. The output power was applied for the time required to reach their melting temperatures, in the case of Cu 2.4s. Analysis of the sample quickly showed if the Si or Cu melted. The time was controlled with a precision better than 0.1 second.

The samples were prepared using a toroidal system similar to that described in Chapter III, however the cell assembly was slightly different than that described in that chapter. Instead of using the assembly depicted in Figure 17, the samples were prepared in a matter similar to Figure 35. The molybdenum ring and plates provided an electrical connection between the anvils and the graphite heater. The CsCl+ZrO_2 is a pressure medium. The ZrO_2+graphite and the ZrO_2 discs act as a thermo isolation medium. The

most important difference is the use of the Zr foil to separate the diamond powder from graphite disc and heater. This ensured that any graphite found in the sample would have originated from graphitization of the diamond powder.

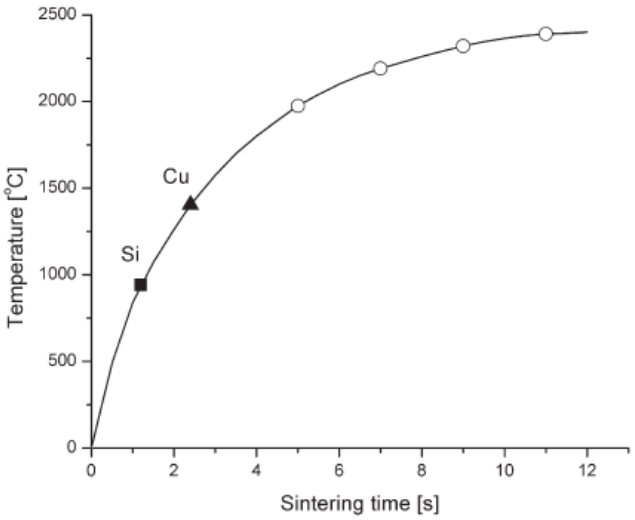

Figure 34 – The temperature curve that the samples followed while being sintered. The square and triangle denote the melting points of Si and Cu, respectively, at 8 GPa.

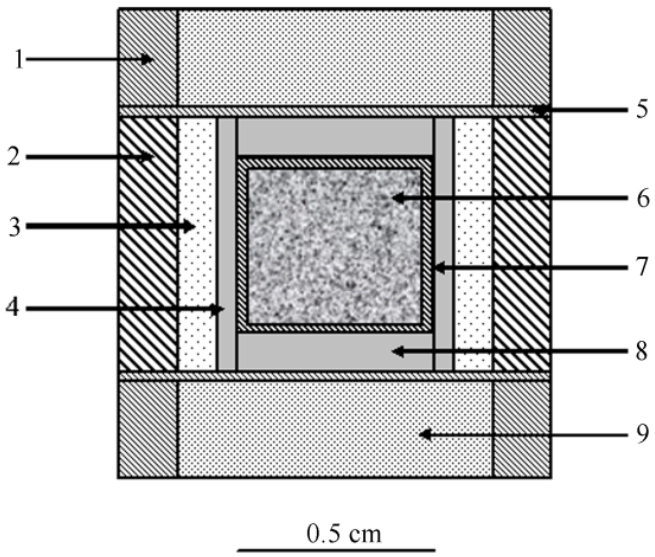

Figure 35 – A cross section of the cell assembly for the high pressure high temperature production of the diamond compacts. (1) Mo ring; (2) CsCl+ZrO_2 (20 wt.%); (3) ZrO_2+graphite (10 vol.%); (4) graphite heater; (5) Mo plate; (6) diamond nanopowder; (7) Zr foil; (8) graphite disc; (9) ZrO_2 disc.

Because the selection rules of the diamond structure factor limit the amount of diamond diffraction peaks, see Equation (3-4), a synchrotron source with a smaller wavelength was used for the x-ray diffraction data. Measurements were taken at the NSLS beam X16C which had a wavelength of 0.06979 nm. Diffraction data were taken from a 2θ range of 13.8^{o} to 78.3^{o} and a step size of 0.001^{o} and an average time per step of 1 second. This allowed 9 peaks to be simultaneously analyzed using the eCMWP method, a Cu anode would only have allowed 4 peaks to be analyzed.

Even though the sintering times were very short there was still graphitization of the diamonds. Analysis of the x-ray diffraction data showed a graphite peak indicating that graphite was present in each sample. By comparing the area under the curve for the *002* diffraction peak of graphite and for the *111* diamond peak we were able to estimate that graphite accounted for less than 2% of the samples volume. Because the diamond powder was isolated from the graphite heater and discs it was assumed that all the graphite present originated from graphitization. Qian, et al. found that most graphitization in micron-sized diamonds takes place in the first 30 minutes of sintering. They also found that the process is much more rapid in nano-sized diamond powders, less than 60 seconds. Because of the volume of pores between the crystal grains, graphitization could not be avoided. Pressure reduces graphitization but the exposed surfaces at the pores are not pressurized and quickly become graphitized at high temperatures. As was mentioned before, the nano-diamonds seem to resist the breaking found in micron-diamonds. They therefore have many more pores between the crystals; and the crystals are not under hydrostatic conditions. After sintering the porosity of the diamond compacts was measured and found to be 16% and

11% for the 5 and 11 second samples respectively. The large porosity coincides with the graphitization of the diamonds even though the sintering times were very short. It is likely that the lower porosity of the 11 second sample was due to an increase in graphite or amorphous carbon. The increase in temperature and time most likely led to an increase in non-diamond carbon. The non-diamond carbon is softer and would be more likely to fill the holes between crystals. Thus there would be a lower porosity.

The eCMWP method was used to analyze the microstructure of diamonds in diamond compacts. The results from the sample sintered at 5 and 11 seconds can be found in Table 5. The eCMWP method was run assuming intrinsic and extrinsic stacking faults and twins. The square sum of the residuals was least when twins were assumed. Therefore when I discuss planar faults in the diamond compacts I will be refer to twins. The planar fault probability was below 1% for both samples. A low planar fault probability is not unusual for diamonds. As the sintering time increased the average crystallite size stayed within repeatability of each other. Both the dislocation density and planar fault probability decrease as the sintering time increases. Annealing of defects has been previously observed with nano-sized diamonds.[40] However, as the results indicate the defect annealing takes time which would result in larger graphite concentration in the nanometer sized diamonds. Despite the presence of graphite and a larger than desired porosity the compacts had a high hardness. The measured Knoops hardness for the samples was 49 ± 3 and 52 ± 2 for the 5 and 11 second samples respectively.

Table 5 – The calculated microstructure parameters of the of the diamond compacts for two different sintering times.

Sintering time [s]	5	11
Porosity [%]	16 ± 1	11 ± 1
Average crystallite size [nm]	16 ± 2	17 ± 2
Stacking fault probability [%]	1.0 ± 0.1	0.50 ± 0.05
Dislocation density [m^{-2}]	$5.3\times10^{15} \pm 0.5\times10^{15}$	$4.2\times10^{15} \pm 0.4\times10^{15}$

This study showed that it is possible to produce very hard nano-diamond compacts by very rapid sintering.

5.2. Diamond in Diamond Composites

The diamond compacts can be quite brittle. Therefore for industrial applications it is important to have the diamonds embedded in a matrix. Often the matrix used is SiC. That is why diamond-SiC composites were also studied. Composites were made using nano-diamond powder and micron-diamond powder.

5.2.1. Diamond in Nano-Diamond-SiC Composites

Nano-diamonds possess high hardness but the compacts produced from them are prone to graphitization. In addition to creating a SiC matrix in order to reduce the brittleness, silicon was used to close pores and stop graphitization.

As mentioned in section 4.2.1. nano-diamond-SiC composites were produced using nano-diamond powder with a size of less than 50 nm and Si powder with a nominal grain size of 30 nm. They were sintered at 8 GPa and temperatures of 1820, 1975, 2190 and 2320 ^{o}C. The diamond to Si ratio was 7:3 by weight. The percent of Si by volume for composites is usually much lower. Since there was more Si and thus a higher concentration of SiC in the composites the hardness of these composites was about half that of what is considered a good superhard composite. The powders were mixed before sintering but due to the agglomeration of the nano-diamond powder there were non-uniform regions in the composites. This led to varying hardness throughout the composites. This in conjunction with fact that the composites cannot be considered superhard materials limits their industrial applications, but they are an important scientific study none the less.

The eCMWP method was used to analyze the microstructure of the diamond phase in these composites. The results of that analysis can be found in Table 6. X-ray diffraction data were taken using beam X14A at the NSLS. The wavelength was 0.080532 nm. The eCMWP method can only analyze one phase at a time. Because of overlapping diamond and SiC peaks analysis was simultaneously done on only 4 diamond peaks. This is still twice more than would have been available if a Cu anode was used.

One can see that as the sintering temperature increases the crystallite size also increases. As with the other samples the eCMWP method was run assuming intrinsic and extrinsic stacking faults and twins. The square sum of the residuals was smallest when

twins were assumed. There is decrease in planar fault probability as the sintering temperature increases. As with the diamond compacts the planar fault probability was very low. The planar fault probability was below 3% for each sample and less than 0.5% for two of them. As the sintering temperature increases there is a decrease in the planar fault probability. The dislocations density decreases with increasing temperature for the three lowest temperatures and then increases for the fourth.

Table 6 – The calculated parameters of the microstructure of diamond in the nano-diamond-SiC composites sintered at 8 GP and various temperatures. $\langle x \rangle_{area}$ is the area-weighted mean crystallite size, β is the planar fault probability, and ρ is the dislocation density.

Temperature (^{o}C)	
1820	$\langle x \rangle_{area} = 20 \pm 2\text{nm}$ $\beta = 2.6 \pm 1\%$ $\rho = 4.3 \pm 1 \times 10^{15}\,\text{m}^{-2}$
1975	$\langle x \rangle_{area} = 24 \pm 2\text{nm}$ $\beta = 1.4 \pm 0.5\%$ $\rho = 0.34 \pm 0.1 \times 10^{15}\,\text{m}^{-2}$
2190	$\langle x \rangle_{area} = 30 \pm 3\text{nm}$ $\beta = 0.2 \pm 0.1\%$ $\rho = 0.13 \pm 0.1 \times 10^{15}\,\text{m}^{-2}$
2320	$\langle x \rangle_{area} = 34 \pm 3\text{nm}$ $\beta = 0 \pm 0.02\%$ $\rho = 0.45 \pm 0.2 \times 10^{15}\,\text{m}^{-2}$

Previous experiments have shown that the dislocation density in ceramics like diamond and SiC increases up to 1800 ^{o}C.[28-31] This would indicate that higher temperatures are needed to initialize dislocation movement or plasticity. The results from this study indicate that at temperatures even higher than 1800 ^{o}C dislocations and planar

faults begin annealing. Since in addition to the annealing the grain size increases, it is assumed that either recovery of the crystal or re-crystallization is occurring. This corresponds to the brittle nature of diamonds at lower temperatures, then as temperatures increase plastic deformation is allowed to set in, and then finally there is re-crystallization.

The alp method was also used to analyze the diamond phase of the nano-diamond-SiC composites, see Table 7. Recall that for a cubic crystal $c_{0,trig} / a_{trig} \approx 0.8165$. The EClp parameter for the initial diamond powder was found to be 3.5659 Å. By comparing this value to the measured EClp values of the composites we can see that the lattice is most expanded in the core of the composite sintered at the lowest temperature. As the sintering temperature increases the EClp value decreases, which corresponds to a shrinking lattice. The EClp value of the 3 composites sintered at the highest temperatures is less than the EClp value of the powder. This would indicate that the cores are compressed relative to the powder. It was not possible to distinguish the interatomic spacing between the core atoms and the shell atoms in the the sample sintered at 1975 ^{o}C. The sample sintered at a temperature lower than 1975 ^{o}C had a smaller interatomic spacing in the shell than in its core. The two samples sintered above 1975 ^{o}C had a larger interatomic spacing in their shells than in their cores. For all three samples were the cores and shells could be distinguished the shell thickness was 5 Å. By comparing the $c_{0,trig} / a_{trig}$ ratio one can see that the amount of planar defects is minimal and does not change drastically for any of the samples. This is similar to the results found from the eCMWP method.

Table 7 – Parameters found from the alp method of the diamond in the nano-diamond-SiC composites. $V_{unit\ cell}$ is the volume of the unit trigonal lattice, s_o is the thickness of the surface shell, and $\Delta r/r$ is the relative change in the interatomic distances in the surface shell.

Temperature (°C)	a_{trig} (Å)	$c_{0,trig}$ (Å)	$c_{0,trig} / a_{trig}$	$V_{unit\ cell}$ (Å^3)	EClp (Å)	s_0 (Å)	$\Delta r / r$ (%)
1820	2.5235	2.0624	0.8173	45.49	3.5698	5	-3
1975	2.5220	2.0559	0.8165	45.30	3.5648	…	…
2190	2.5195	2.0592	0.8173	45.28	3.5642	5	+1
2320	2.5190	2.0589	0.8173	45.26	3.5639	5	+3

5.2.2. Diamond in Micron-Diamond-SiC Composites

Composites were sintered using micron-sized diamonds and Si powder. The samples were sintered using natural diamond powder with a grain size of 50 – 70 μm and Si powder with a particle size of 30 nm. The sintering pressure was 10 GPa and the temperatures were 1600, 1800, and 2000 °C. Unlike the nano-diamond-SiC composites the powders were not premixed before sintering. Also the powders had an 85:15 diamond to Si weight ratio. These composites therefore did not suffer the same problems that affected the nano-diamond-SiC composite's hardness. The Knoops hardness was measured to be above 40 GPa for each sample. In addition to the 3 composites a diamond compact was made from the same starting material and it was sintered at 10 GPa and 2000 °C.

A Williamson-Hall plot of the diamond phase was made. It did not show order dependence however it did show an increase in the full width for half maximum as an increase in the diffraction vector. This would seem to indicate that there were few planar

faults and that the primary sources of peak broadening were due to crystallite size and dislocation density. The eCMWP method was performed on the four samples made from the micron-sized diamonds. The results can be found in Table 8. The planar fault probability was found to 0% for each sample and therefore was not listed in this table.

Table 8 – The calculated parameters of the microstructure of the diamond in the micron-diamond-SiC composites and compact sintered at 10 GPa and various temperatures: $\langle x \rangle_{area}$ is the area-weighted mean crystallite size and ρ is the dislocation density.

Temperature (^{o}C)	
1600	$\langle x \rangle_{area} = 210 \pm 20\text{nm}$ $\rho = 0.082 \pm 0.007 \times 10^{15}\,\text{m}^{-2}$
1800	$\langle x \rangle_{area} = 200 \pm 20\text{nm}$ $\rho = 0.092 \pm 0.009 \times 10^{15}\,\text{m}^{-2}$
2000	$\langle x \rangle_{area} = 180 \pm 20\text{nm}$ $\rho = 0.12 \pm 0.01 \times 10^{15}\,\text{m}^{-2}$
Compact	$\langle x \rangle_{area} = 80 \pm 8\text{nm}$ $\rho = 0.15 \pm 0.02 \times 10^{15}\,\text{m}^{-2}$

The diamond compact has a significantly smaller crystallite size than any of the composites. Recall that the crystallite size is the domains of the crystals that scatter coherently. There may be tens to even thousands of crystallites in a single crystal. Crystallites may be separated by dislocations which will not be visible to SEMs. Therefore the best way known to us to measure crystallite sizes is with the eCMWP method. As the sintering temperature increases the average crystallite size decreases.

In the composites as the sintering temperature increases the dislocation density increases. The compact has the largest population of dislocations. This taken in addition with fact that the compact has the smallest crystallite size seems to indicate the binding phase, SiC, when it filled the spaces between the diamond crystals stopped the further deformation of the diamond crystals. This would reduce the amount of dislocations and reduce the amount of cracks.

The planar fault probability was very low, below the detectable amount by the eCMWP method. Finding diamonds without planar faults is not unusual. The nano-diamond-SiC composite sintered at the highest temperature had a planar fault probability of 0% and of the 10 measured samples that contained diamond only 2 had planar fault probabilities above 1%.

CHAPTER VI. CONCLUSIONS

There is a correlation between the average crystallite size and the sintering temperature in the SiC compacts and the composites made with the nano-sized diamonds. For a fixed pressure as the temperature increases the average crystallite size increases, see Tables 1 and 2. This trend however reverses for the composites sintered with the micron-sized diamonds. There the crystallite size decreases as the sintering temperature increases. A viable explanation for this reverse in trend cannot be offered. The composites sintered with the micron-sized diamonds were made at 10 GPa. Crystallite growth is directly dependent on sintering temperature and pressure, but it is also dependent on factors such as compressibility and the thermal expansion coefficient of both phases. At normal conditions SiC has a larger thermal expansion coefficient than diamond, but at 1600 ^{o}C the values of the thermal expansion coefficients seem to converge. Only limited data on thermal expansion coefficients of diamond and SiC are available at high pressure. But data obtained from computer simulations[41] and some experimental results obtained by L. Balogh et al.[42] indicate that differences in thermal expansion coefficients are responsible for the observed stress.

In all of the samples the predominate form of planar fault was the twin. This was observed visually in TEM images and using the eCMWP fitting method which had a smaller sum of residual when run using twins as opposed to extrinsic or intrinsic stacking faults. For the SiC compacts we found that there was a correlation between the crystallite

size and the planar fault probability. This trend was observed in the composites as well, see Figure 36. Crystallites with an average grain size of less than 60 nm have an order magnitude higher fault probability than crystallites with an average grain size larger than 60 nm. A larger crystallite has more atomic planes. Planar faults change the distances between atomic planes and thus their formation requires external energy. As the number of atomic planes in a crystallite increases the required energy also increases. This could explain why larger crystallites have a smaller planar fault probability.

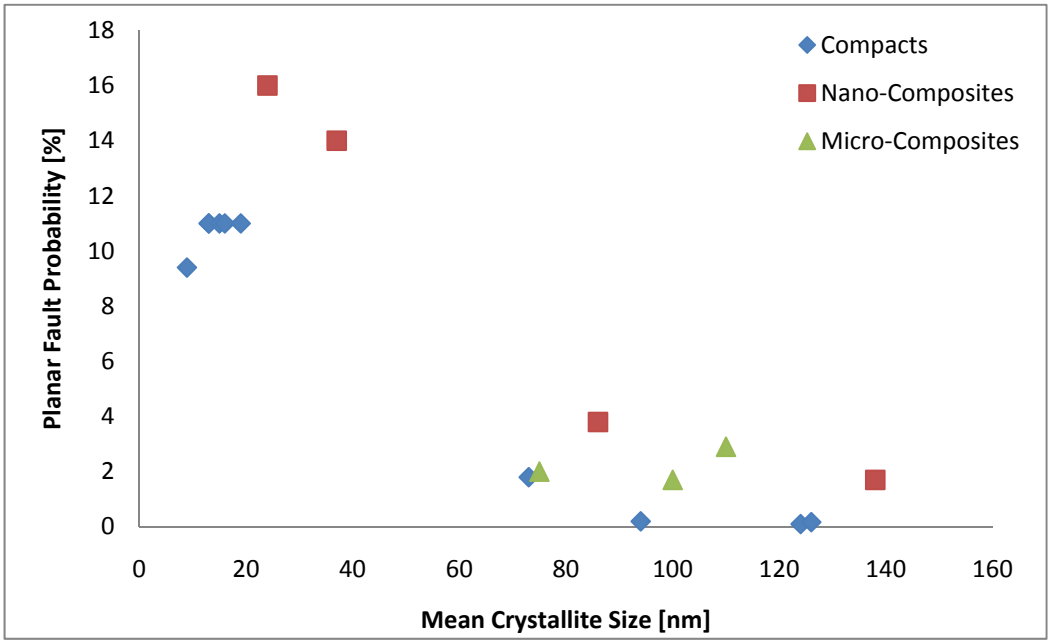

Figure 36 – A plot of the mean crystallite size versus the planar fault probability for the SiC phase of the nano and micron-sized diamond composites and the compacts.

Zhu et al.[43] found in Cu that crystals with small crystallite sizes predominately had planar faults and above a certain crystallite size severe plastic deformation activates dislocations. A similar trend was observed for SiC, see Figure 37. As the crystallite size

increases it appears that the formation of dislocations is preferred to stacking faults. This threshold occurs between 25 and 75 nm.

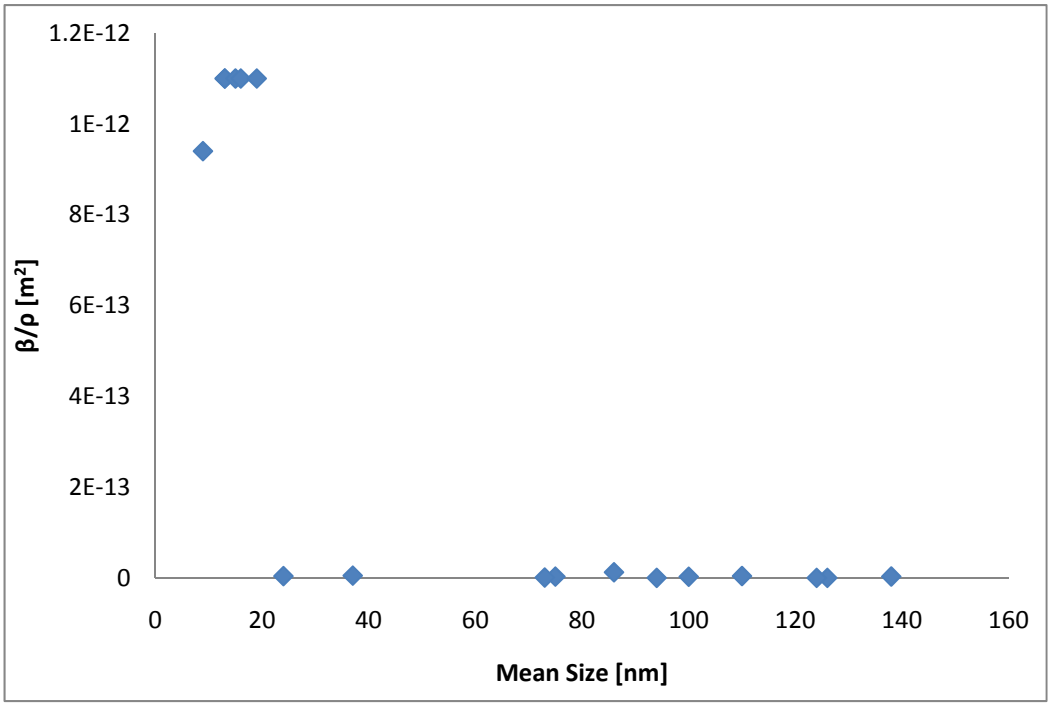

Figure 37- The ratio of planar fault probability to dislocation density (β/ρ) as a function of the mean crystallite size for all the SiC samples.

As the sintering temperature increased the mean crystallite size of the diamonds of the nano-meter sized composites also increased. There was also decrease in the dislocation density as the mean crystallite size increased. This observation indicates that recrystallization took place. The mean crystallite size of the compacts made from the nano-meter diamonds remained unchanged. However, there was a decrease in the dislocation density. In both composites and compacts there were planar faults present and the amount of faults decreased as temperature increased. However, there were far fewer faults in the diamond than in the SiC samples.

The diamond phase in the micron-sized diamond composites had a different correlation between sintering temperature and mean crystallite size than in the nano-sized diamond composites. In the micron-sized composites there was a decrease in crystallite size as the sintering temperature increased. Since these composites were sintered at 10 GPa (as opposed to 8 GPa) it is possible that at 10 GPa higher temperatures are needed for recrystallization to occur. The dislocation density also increased as the sintering temperature increased. But the density was much lower than that in the nano-sized diamonds. There was also no appreciable amount of stacking faults found by the eCMWP analysis in the micron-sized diamonds. This finding indicates that the defects in diamond phase can be affected by sintering conditions and the size of the initial crystals.

The compact that was created using the same micron-sized diamond powder had a smaller crystallite size and more dislocations than its composite counterpart. This result was explained by the presence SiC, which, when it fills the gaps between the diamond crystals, acts as a buffer between the crystals to reduce strain and deformation to the diamond.

Stress is present in both phases. Its origin is in different thermal expansions and compressibility of the two phases and at the atomic level can be explained in terms of different lattice constants in the interior and exterior layers of the crystallites. The alp method, which was used to analyze the atomic level, could only be applied to the nanometer-sized diamond-SiC composites.

When the ratio of the shell's interatomic differences, $\Delta r / r$, are less than zero it implies that the distances in the shell are less than the distances in the core. In other words that the shell atoms are more compressed and that the core atoms are more relaxed. Therefore, the strain is concentrated in the shell. The diamond phase in the nano-sized diamond composites had a negative $\Delta r / r$ ratio in the sample sintered at the lowest temperature. The sample sintered at 1975 ^{o}C had no distinguishable difference in the atomic spacings between the core and shell atoms; an indication that the diamond crystals have uniform strain. Above that temperature the ratio changes sign and the shell is less compressed than the core. In the SiC phase however, the samples sintered at the two lowest temperatures have compressed shells. The sample sintered at 2190 ^{o}C has no distinguishable differences in the core and shell atomic spacings. But when the temperature was increased to 2320 ^{o}C we discovered that the core was compressed more than the shell. This indicates that during sintering at certain specific temperature and pressure values the diamond and the SiC crystals both become relaxed. Unfortunately this occurs at different temperatures for the diamond and the SiC phase. It is therefore impossible to create a diamond SiC composite that is completely free of strain. This conclusion is limited to the sintering pressure of 8 GPa. However, it is possible that different pressures may produce samples that will be strain free in both phases for some yet unknown common temperature. But users of commercially manufactured nanocomposites sintered at 8 GPa must decide, based on the future application, if it is of more value to have a weaker SiC matrix and strain free diamond crystals or a stronger SiC matrix but diamond crystals with large surface strain.

References

1. I.E. Clark, P.A. Bex, Ind. Diamond Rev. 59 (1999) 560.

2. P.N. Tomlinson, J.J. Pipkin, A. Lammer, R.P. Burnand, Ind. Diamond Rev. 45 (1985) 299.

3. G. Burns, Solid State Physics, Academic Press, Inc, New York, 1985.

4. C. Hammond, The Basics of Crystallography and Diffraction, Oxford University Press, New York, 2001.

5. B.D. Cullity, Elements of X-ray Diffraction, Addison-Wesley Pub. Co., Massachusetts, 1956.

6. C. Kittel, Introduction to Solid State Physics, Wiley, New York, 1995.

7. B.E. Warren, X-ray Diffraction, Dover, New York, 1990.

8. Y. Quere, Physics of Materials, Gordon and Breach Science Publishers, Canada, 1998.

9. T. Ungar, Mater. Sci. and Engineering A, 309-310, (2001) 14.

10. G. Ribarik, T. Ungar, J. Gubicza, J. Appl. Cryst. 34 (2001) 669.

11. L. Balogh, G. Ribarik, T. Ungar, J. Appl. Phys. 100 (2006) 023512.

12. E.F. Bertaut, Acta Cryst. 3 (1950) 14.

13. A. Guinier, X-ray diffraction, Freeman, San Fransico, 1963.

14. T. Ungar, J. Gubicza, G. Ribarik, T.W. Zerda, Mat. Res. Soc. Symp. 661 (2001) KK9.2.1.

15. B.E. Warren, B.L. Averbach, J. Appl. Phys. 23 (1952) 497.

16. M.A. Krivoglaz, Theory of X-ray and thermal neutron scattering by real crystals, Plenum, New York, 1969.

17. M. Wilkens, Fundamental aspects of dislocation theory, Vol. II., edited by J.A. Simmons, R. de Wit and R. Bullough. NBS Spec. Publ. 317, 1195 (1970).

18. T. Ungar, G. Tichy, Phys. Status Solidi A 171 (1999) 425.

19. M.M.J. Treacy, J.M. Newsam, M.W. Deem, Proc. Roy. Soc. Lond. A 433 (1991) 499.

20. L. Balogh, G. Ribarik, T. Ungar, J. Appl. Phys. 100 (2006) 023512.

21. B. Palosz, S. Stelmakh, S. Gierlotka, Z. Kristallogr. 210 (1995) 731.

22. S. Stelmackh,. Ph.D. thesis, Warsaw University, (1997).

23. B. Palosz, S. Stelmakh, E. Grzanka, S. Gierlotka, S. Nauyoks, T.W. Zerda, W. Palosz, J. Appl. Phys. 102 (2007) 074303.

24. Yu A. Vodakov, G.A. Lomakina, E.N. Mokhov, Sov. Phys. Solid State 24 (1982) 280.

25. R. Gold'shmidt, Yu. M. Tairov, V.F. Tsvetkov, M.A. Chernov, Sov. Phys. Solid State 27 (1982) 371.

26. Y.T. Zhu, J.Y. Huang, J. Gubicz, T. Ungar, Y.M. Wang, E. Ma, R.Z. Valiev, J. Mater. Res. 18 (2003) 1908.

27. K. Koumoto, S. Takeda, Ch.H. Pi, T. Sato, H. Yanagida, J. Am. Ceram. Soc. 72 (1989) 1985.

28. G.A. Voronin, T.W. Zerda, J. Qian, Y. Zhao, D. He, S.N. Dub, Diamond Relat. Mater. 12 (2003) 1477.

29. J. Gubiza, T. Ungar, Y. Wang, G. Voronin, C. Pantea, T.W. Zerda, Diamond Relat. Mater. 15 (2006) 1452.

30. C. Pantea, J. Gubicza, T. Ungar, G.A. Voronin, T.W. Zerda, Phys. Rev. B. 66 (2002) 094106.

31. J. Gubicza, S. Nauyoks, L. Balogh, J. Labar, T.W. Zerda, T. Ungar, J. Mater. Res. 22 (2007) 1314.

32. P. Keblinski, D. Wolf, S.R. Phillpot, H. Gleiter, Philos. Mag. Lett. 76 (1997) 143.

33. T. Yamamoto, H. Kitaura, Y. Kodera, T. Ishii, M. Ohyanagi, Z.A. Munir, J. Am. Ceram. Soc. 87 (2004) 1436.

34. F. Liao, S.L. Girshick, W.M. Mook, W.W. Gerberich, M.R. Zachariah, Appl. Phys. Lett. 86 (2005) 171913.

35. G.N. Yushin, S. Osswald, V.I. Padalko, G.P. Bogayreva, Y. Gogotsi, Diamond Relat. Mater. 14 (2005) 1721.

36. Y.G. Gogotsi, A. Kailer, K.G. Nickel, J. Appl. Phys. 84 (2998) 1299.

37. J. Qian, C. Pantea, G. Voronin, T.W. Zerda, J. Appl. Phys. 90 (2001) 1632.

38. Iy.E. Geguzin, Sintering Physics, Nauka, Moscow 1967.

39. B. Palosz, C. Pantea, E. Grzanka, S. Stelmakh, Th. Proffen, T.W. Zerda, W. Palosz, Diamond Relat. Mater. 15 (2006) 1813.

40. G.A. Voronin, Proceedings of Joint AIRAPT-16 & HPCj-38 Int. Conf., Jap Soc. High Pressure Sci. Technol. Kyoto, Japan, vol. 467, (1997).

41. J. Xie, S.P. Chen, J.S. Tse, S. Baroni, Phys. Rev. B 60 (1999) 9444.

42. L. Balogh, S. Nauyoks, T.W. Zerda, C. Pantea, S. Stelmakh, B. Palosz, T. Ungar, Mater. Sci. Eng. A 487 (2007) 180

43. Y.T. Zhu, X.Z. Liao, S.G. Srinivasan, E.J. Lavernia, J. Appl. Phys. 98 (2005) 034319.

ABSTRACT

Microstructure of nano and micron diamond-SiC Composites sintered under high pressure high temperature conditions

by Stephen Edwin Nauyoks, Ph. D., 2009
Department of Physics and Astronomy
Texas Christian University

Dissertation Advisor:
Dr. T.W. Zerda, Professor of Physics

Compacts and composites were sintered under high pressure (2 GPa – 10 GPa) and high temperature (1400 – 2300 ^{o}C) conditions. The compacts were sintered using nano-SiC powder, micron-diamond powder, and nano-diamond powder. Composites were sintered using the liquid infiltration method from nano-silicon powder and nano or micron diamond powder. Under the high pressure, high temperature conditions the silicon powder would melt and react with carbon from the diamonds to form a SiC matrix.

The microstructure and strain of the composites and compacts was analyzed using X-ray diffraction analysis. The extended convolutional multiple whole profile fitting method was used to analyze the X-ray line profiles to determine average crystallite size, dislocation density, and planar fault probability. The apparent lattice parameter method was used to analyze strain. Below a certain pressure there was subgrain growth. However, at the higher pressures there was a reduction in crystallite size. In the SiC phase there was a correlation between predominate defect, dislocation or planar fault, and the crystallite

size. The defect structure of the diamonds seemed to be dependent on the initial diamond powder used. At higher temperatures there was evidence of recovery and or recrystallization.

VITA

Stephen Edwin Nauyoks

Education

Texas Christian University, Fort Worth, TX 2009
Ph.D. Physics
Thesis: Microstructure of nano-diamond-SiC composites sintered under high pressure high temperature conditions
NSF Research Assistantship

New Jersey Institute of Technology, Newark, NJ 2004
M.S. Applied Mathematics

New Jersey Institute of Technology, Newark, NJ 2002
B.S. Applied Mathematics
Minor: Science, Technology, and Society
Albert Dorman Honors College

Publications

S. Nauyoks, M. Wieligor, T.W. Zerda, L. Balogh, T. Ungar, P. Stephens: Stress and dislocations in diamond-SiC composites sintered at high pressure, high temperature conditions, *Compos. Part A-Appl. S.*, Article in Press

A.S. Osipov, S. Nauyoks, T.W. Zerda, O. Zaporozhets: Rapid sintering of nano-diamond compacts, *Diam. Relat. Mater.*, Article in Press

L. Balogh, S. Nauyoks, T.W. Zerda, C. Pantea, S. Stelmakh, B. Palosz, T. Ungar: Structure of diamond silicon carbide nanocomposites as a function of sintering temperature at 8 GPa. *Mater. Sci. Eng. A*, **487**, 180 (2008)

B. Palosz, S. Stelmakh, E. Grzanka, S. Gierlotka, S. Nauyoks, T. W. Zerda, W. Palosz: Origin of macrostrains and microstrains in diamond-SiC nanocomposites based on the core-shell model. *J. Appl. Phys.*, **102**, 074303 (2007)

J. Gubicza, S. Nauyoks, L. Balogh, J. Labar, T.W. Zerda, T. Ungár: Influence of sintering temperature and pressure on crystallite size and lattice defect structure in nanocrystalline SiC. *J. Mater. Res.*, **22**, 1314 (2007)

Research Experience

X-ray analysis using Philips X'pert, rotating anodes, and synchrotron sources
High Pressure High Temperature synthesis, using piston and toroidal systems
Induction Furnace
AFM, SEM, FTIR, Raman